Supplementary Information (SI) for Journal of Materials Chemistry A.

Supplementary information

Low-Voltage Paired Electrolysis via MOF-Derived Hierarchical Pt-Cu Electrocatalysts for Integrated Hydrogen Production and Chemical Upgrading

Seunghyeon Choi,[†a] Jaegeol Kim,[†b] Jinwon Choi,[a] Hyeyoung Shin*[bc] and Seonggyu Lee*[a]

[a]Department of Chemical Engineering, Kumoh National Institute of Technology (KIT), Gumi 39177, Republic of Korea
[b]Graduate School of Energy Science and Technology (GEST), Chungnam National University, 99 Daehak-ro, Yuseong-gu, Daejeon 34134, Republic of Korea
[c]Department of Chemistry, College of Sciences, Kyung Hee University, Seoul 02447, Republic of Korea

[†]S. Choi and J. Kim contributed equally to this work.

*Corresponding authors: shinhy@khu.ac.kr (H. Shin), seonggyulee@kumoh.ac.kr (S. Lee)

Experimental Procedures

Chemical and materials

Commercial copper foam sheet (MTI Korea), Nafion Membrane NR-212(Dupont), N,N-Dimethylformamide (C_3H_7NO, DAEJUNG), Cobalt(II) nitrate hexahydrate ($Co(NO_3)_2 \cdot 6H_2O$, Sigma-Aldrich), Platinum(II) acetylacetonate ($Pt(C_5H_7O_2)_2$, Sigma-Aldrich), Ammonium persulfate ($(NH_4)_2S_2O_8$, Sigma-Aldrich), Terephthalic acid (C_6H_4-1,4-$(CO_2H)_2$, Sigma-Aldrich), Sodium hydroxide beads (NaOH, DAEJUNG), Potassium hydroxide (KOH, 1 M, SAMCHUN), Furfural ($C_5H_4O_2$, Sigma-Aldrich), Furfuryl alcohol ($C_5H_6O_2$, Sigma-Aldrich), Formaldehyde solution (HCHO, 37 wt. % in H_2O, contains 10-15% Methanol as stabilizer, Sigma-Aldrich), Ammonium acetate ($CH_3CO_2NH_4$, Sigma-Aldrich), Acetylacetone ($CH_3COCH_2COCH_3$, Sigma-Aldrich), Acetic acid (CH_3COOH, DAEJUNG), Hydrochloric acid (HCl, DAEJUNG), Potassium formate (HCOOK, ThermoFisher,), Formic acid (HCOOH, TCI), Methanol (CH_3OH, DAEJUNG), Paraformaldehyde-d_2 ($(CD_2O)_n$, 98 atom %D, Sigma-Aldrich), PiperION membrane (20 µm, Versogen)

Synthesis of $Cu(OH)_2$ nanowire

First, the Cu foam was purified by sonicating in ethanol and agitating in 1 M HCl for 15 min each. Then, it was rinsed multiple times with deionized water and dried using an air stream. Afterward, it was immersed in an aqueous solution (40 mL) containing 3.2 g of NaOH and 1 g of ammonium persulfate for 10 minutes. The resulting product was washed several times with deionized water and dried to obtain $Cu(OH)_2$ nanowires.[1]

Synthesis of Cu-MOF and M-Cu-MOF (M=Co, Pt)

The Cu-MOF was prepared through a solvothermal reaction. Specifically, the synthesized $Cu(OH)_2$ was placed in a dimethylformamide solution (30 mL) containing 1.0 g of terephthalic acid and reacted at 100°C for 10 hours. After gradual cooling, the resulting product was rinsed multiple times with dimethylformamide solution and dried to yield Cu-MOF. The synthesis procedure of M-Cu-MOF followed the same steps as Cu-MOF, except that cobalt(II) nitrate hexahydrate (or platinum(II) acetylacetonate) was introduced into the dimethylformamide solution. The Co-Cu-MOF was synthesized using cobalt(II) nitrate hexahydrate at a concentration of 5 mM, while the Pt-Cu-MOF was obtained by incorporating platinum(II) acetylacetonate at a concentration of 5 mM.

Synthesis of Cu and M-Cu (M=Co, Pt)

The pure Cu was produced by subjecting Cu-MOF to heat treatment at 300 °C for 2 hours under a mixed gas flow of 5% H_2/Ar (200 mL min^{-1}). The M-Cu samples were obtained by applying the same heat treatment conditions to M-Cu-MOF.

Characterization

Scanning electron microscopy (SEM) images were obtained using a JEOL (JSM-IT700HR). Transmission electron microscopy (TEM), high-resolution TEM (HR-TEM), high-angle annular dark-field scanning TEM (HAADF-STEM), and energy-dispersive X-ray spectroscopy (EDS) elemental mapping were performed using a JEM-ARM 200F (NEOARM, JEOL) microscope at an accelerating voltage of 200 kV. X-ray powder diffraction (XRD) analysis was performed using a Smartlab (Rigaku) at 45.0 kV and 200 mA with Cu Kα (λ=1.5406Å) radiation. X-ray photoelectron spectroscopy (XPS) analysis was performed using Versaprobe III (ULVAC-PHI), with the carbon 1s peak at 284.6 eV used for calibration. High-performance liquid chromatography (HPLC) analysis was performed using Shimadzu Prominence LC-2030C with a C18 column, 5 µm, 4.6 mm X 250 mm. Ultraviolet-visible (UV-Vis) spectroscopy spectra were obtained using Cary 60 (Agilent). Inductively coupled plasma mass spectrometer (ICP-MS) analysis was performed using a NexlON2000.

Electrochemical measurement

All electrochemical measurements were performed in a typical three-electrode system using the potentiostat (PARASTAT MC, AMETEK) setup with a H-type cell which was separated by Nafion Membrane NR-212. A three-electrode system, in which the pure Cu/CF and M-Cu/CF were used as the working electrode, the platinum sheet was used as the counter electrode, and the Hg/HgO (1 M NaOH) was used as the reference electrode, was used for the electrochemical measurements. Before the FEH and FOR, the pure Cu/CF and M-Cu/CF catalysts were scanned for 10 cycles by cyclic voltammetry (CV) in the potential range of −0.9 to −1.4 V (vs. Hg/HgO) for FEH and −1.0 to −0.4 V (vs. Hg/HgO) for FOR, respectively. Thus, the electrode surface was brought to a stable state, after which CV measurements were conducted. The FEH and FOR were conducted in a 15 mL 1 M KOH solution with 0.03 M furfural and 15 mL 1 M KOH solution with 0.6 M HCHO in H-cell, respectively.

The electrocatalyst activity for FEH and FOR was measured using linear sweep voltammetry (LSV) in the range of −0.9 to −1.4 V (vs. Hg/HgO) at a 10 mV s^{-1} scan rate and in the range of −1.0 to −0.4 V (vs. Hg/HgO) at a 10 mV s^{-1} scan rate, respectively. All LSV data were corrected for ohmic losses using static iR compensation, where the solution resistance (Rs) was determined from electrochemical impedance spectroscopy (EIS) measurements at open circuit potential. The iR-corrected potential was calculated using the equation E−iR, where i is the applied current and R is the measured solution resistance, with 100% compensation applied. The stability of FEH and FOR was measured using chronoamperometry (CA) at a fixed potential value −1.23 V (vs. Hg/HgO) and −0.63 V (vs. Hg/HgO), respectively. The electrolyte of H-cell was refreshed every cycle. The operando Electrochemical impedance spectroscopy (EIS) for the Bode plot for FEH was conducted with an amplitude of 10 mV, within a frequency range of 100 kHz to 10 mHz, and a potential range of −0.93 to −1.23 V (vs. Hg/HgO). The Nyquist plot for FOR was obtained from the EIS test at −0.63 V (vs. Hg/HgO).

The double layer capacitance (C_{dl}) was measured by CV at scan rates ranging from 10 to 50 mV s^{-1} at potentials between −0.75 and −0.65 V (vs. Hg/HgO) to estimate the electrochemical surface area (ECSA). The following equation was used for the calculation:

$$\mathrm{ECSA} = \frac{C_{dl}}{C_s}$$

where C_s values indicated the specific capacitance in different electrolytes. In this study, C_s value of 1.0 M KOH is 0.4 mF cm^{-2}.

All electrochemical measurements versus Hg/HgO were calibrated to the reversible hydrogen electrode (RHE) using the following equation:

$$E_{RHE} = E_{Hg/HgO} + 0.118 + 0.0592 \times \mathrm{pH}$$

where 0.118 V is the standard potential of the Hg/HgO reference electrode (in 1 M NaOH) versus SHE, and 0.0592 × pH accounts for the conversion from SHE to RHE at the experimental pH. In this study, the pH of the 1.0 M KOH electrolyte was measured to be 13.72, giving a total conversion factor of $0.118 + 0.0592 \times 13.72 = 0.93$ V. All potentials reported in the figures and text are presented on the RHE scale unless otherwise stated, and consistency across all figures was verified accordingly.

Product analysis and calculation

The concentrations of furfural (FF) and furfuryl alcohol (FA) were quantified by HPLC both before and after electrolysis. For product analysis, 50 μL of the electrolyte was diluted with 2 mL of deionized water. The detector wavelength was set to 230 nm, with acetonitrile as mobile phase A and ultrapure water as mobile phase B, maintaining an A:B ratio of 1:9. The flow rate was 1 mL min^{-1}, and the separation time for each sample was 17 minutes. The quantification of FF and FA was determined based on calibration curves constructed from standard compounds of known concentrations. The Faradaic efficiency of FA was calculated using the following equation:

$$\text{Faradaic efficiency of FA} = \frac{nFN}{Q_{total}} \times 100\%$$

where n is the number of electrons transferred for FA, F is Faraday constant (96,485 C mol^{-1}), N is the mole number of FA and Q_{total} is the total passed charge.

Formaldehyde concentrations before and after the electrolysis process were quantified using UV-Vis absorption measurements.[2, 3] The UV-Vis spectra used for color development was obtained by dissolving ammonium acetate (7.7 g), acetic acid (150 μL), and acetylacetone (100 μL) in 49.75 mL of deionized water. The concentration of formaldehyde throughout the experiment was determined by acidifying 5.0 μL of formaldehyde solution, both before and after the reaction, with 5.0 μL of 2.0 M HCl, followed by a 2500-fold dilution. Subsequently, 3.0 mL of the diluted solution was combined with 3.0 mL of acetylacetone solution and further heated to 58°C for 10 minutes. After complete cooling, the absorbance of the sample solution was measured at 412 nm. The concentration of HCHO was determined from a calibration curve generated using a standard HCHO solution.

The concentrations of formate ($HCOO^-$) were quantified by HPLC both before and after electrolysis. For product analysis, 1 mL of the electrolyte was acidified with 1 mL of 0.5 M H_2SO_4. The Faradaic efficiency of $HCOO^-$ was calculated using the following equations:

$$\text{Faradaic efficiency of HCOO}^- = \frac{nFN}{Q_{total}} \times 100\%$$

where n is the number of electrons transferred for $HCOO^-$, F is Faraday constant (96,485 C mol^{-1}), N is the mole number of $HCOO^-$ and Q_{total} is the total passed charge.

Computational Details

Spin-polarized density functional theory (DFT) calculations were performed using the Vienna Ab initio Simulation Package (VASP) within a plane-wave basis set.[4-7] Exchange–correlation effects were described using the Perdew–Burke–Ernzerhof (PBE) functional within the generalized gradient approximation (GGA)[8], and the projector-augmented wave (PAW) method was employed to represent the electron–ion interactions.[9] Long-range dispersion interactions were included using Grimme's D3 correction.[8, 10] A plane-wave energy cutoff of 400 eV was used for all calculations. Brillouin-zone integrations were carried out using a Γ-centered 2×2×1 *k*-point mesh.

The pristine Cu surface was modeled as a four-layer Cu (111) slab using a (5×4) surface supercell. Dopant-substituted Cu (111) slab models were constructed by replacing one Cu atom in the topmost layer with a Pt or Co atom, corresponding to the Pt-Cu and Co-Cu surfaces, respectively. A vacuum layer of at least 20 Å was introduced along the surface normal (*z*-direction) to avoid spurious periodic interactions. During structural relaxations, the bottom two atomic layers were fixed to mimic bulk-like behavior, while the upper two layers and all adsorbates were fully relaxed. Structural optimizations were performed until the total energy change between consecutive ionic steps was less than 10^{-4} eV, and electronic self-consistency was achieved within 10^{-5} eV. Transition states (TS) were identified using the climbing image nudged elastic band (CI-NEB) method.[11] Convergence was achieved when the maximum force on each relaxed atom was below 0.03 eV/Å.

Anion exchange membrane (AEM) paired electrolyzer measurement

The AEM paired electrolyzer was configured with a 20 μm-thick PiperION membrane and Pt-Cu/CF as both the cathode and anode. At room temperature, the catholyte (1.0 M KOH + 0.03 M FF) and the anolyte (1.0 M KOH + 0.6 M HCHO) were circulated at a flow rate of 40 mL min^{-1}. For comparison, conventional water electrolysis was also conducted as a control experiment under the identical configuration and operating parameters, except that 1.0 M KOH was employed as the electrolyte for both the cathode and anode sides. Electrochemical performances were evaluated using LSV at a scan rate of 2 mV s^{-1}. For the paired FEH-FOR system, the cell voltage was scanned from the open-circuit potential (OCP) to 0.8 V. In comparison, for the conventional water electrolysis control, the potential was recorded from OCP to 2.0 V. Long-term stability measurements for the paired system were conducted via CA at a constant cell voltage of 0.5 V. For long-term stability measurements, the electrolytes were refreshed every 10 h to maintain optimal catalytic performance during extended measurements.

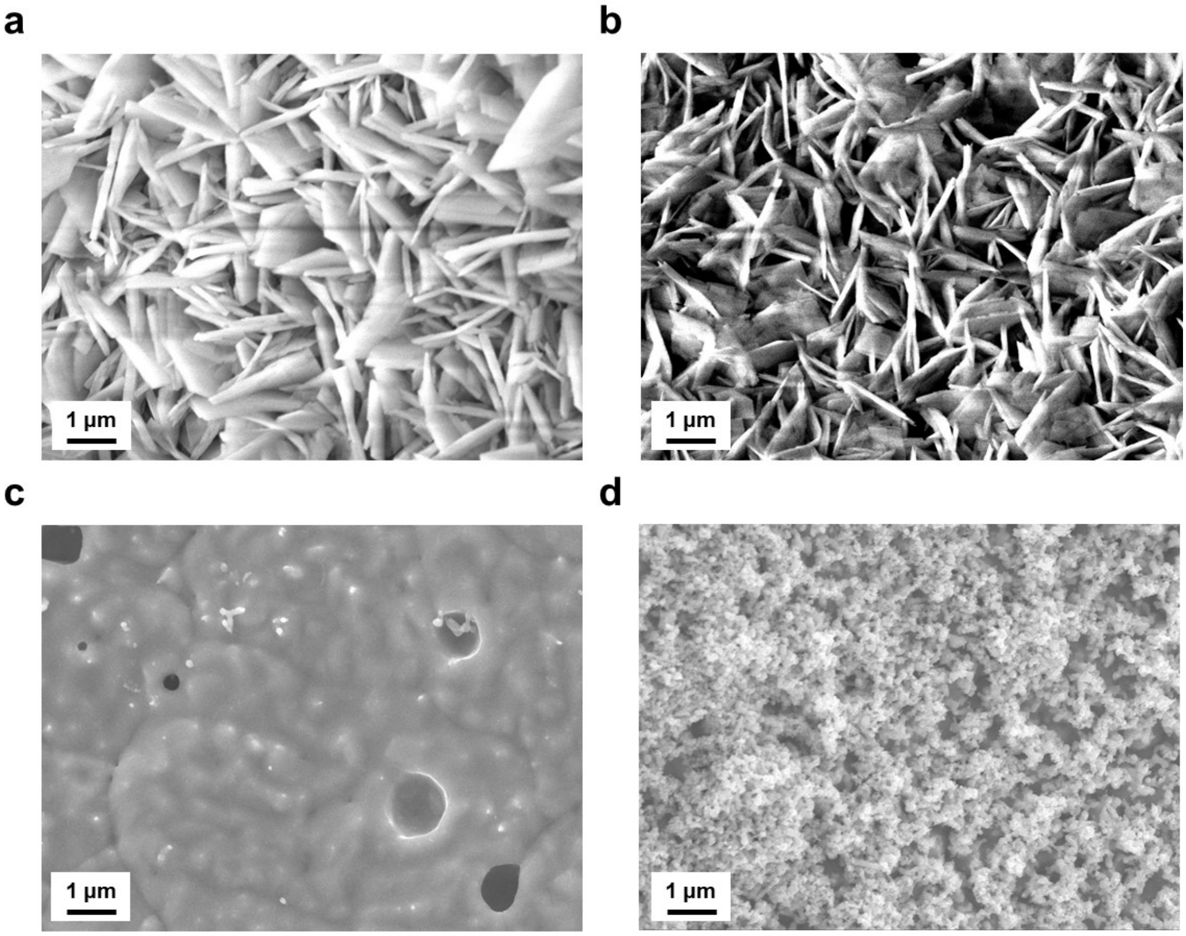

Figure S1. FE-SEM images of (a) Co-Cu-MOF/CF, (b) Pt-Cu-MOF/CF, (c) Co-Cu/CF, and (d) Pt-Cu/CF.

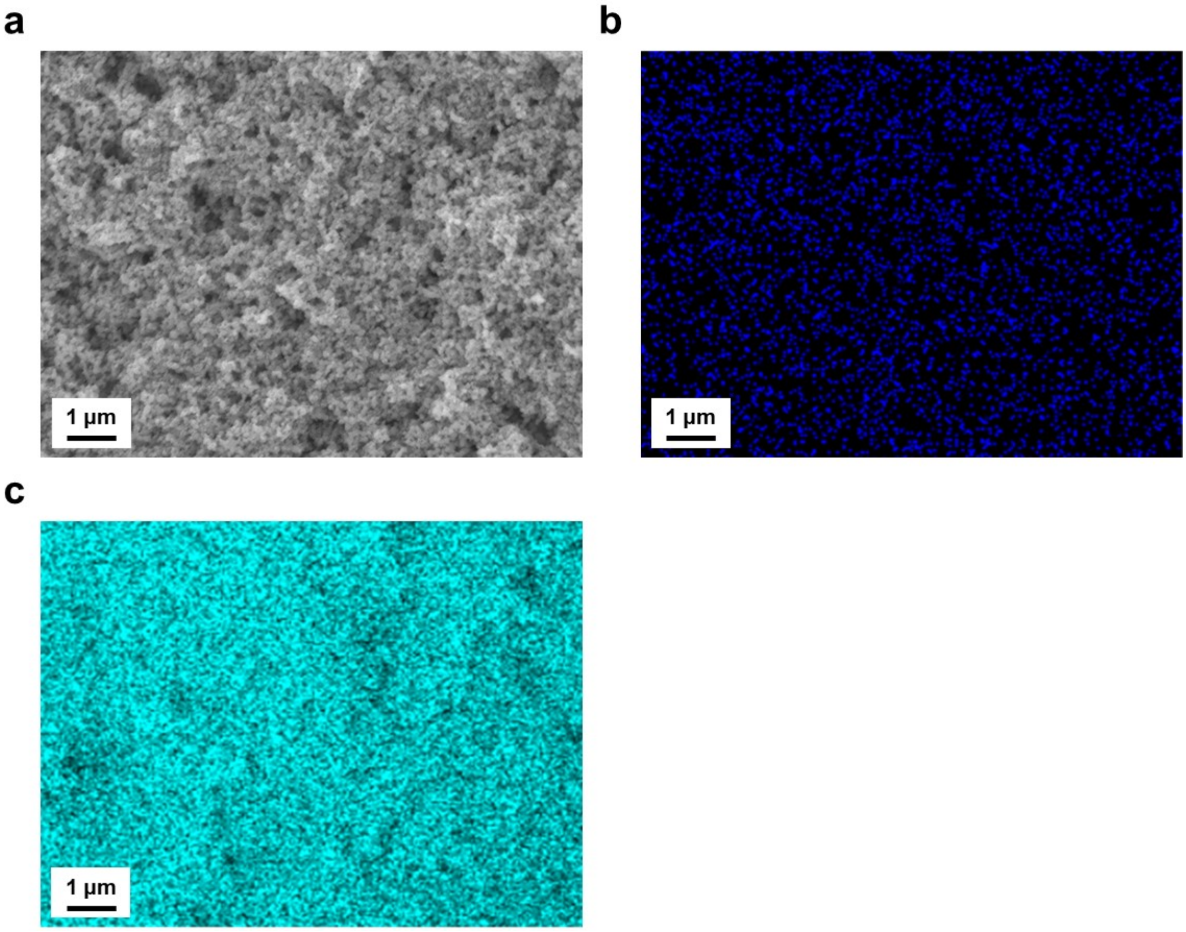

Figure S2. (a) FE-SEM image, and corresponding EDS elemental mapping of (b) Pt and (c) Cu of Pt-Cu/CF.

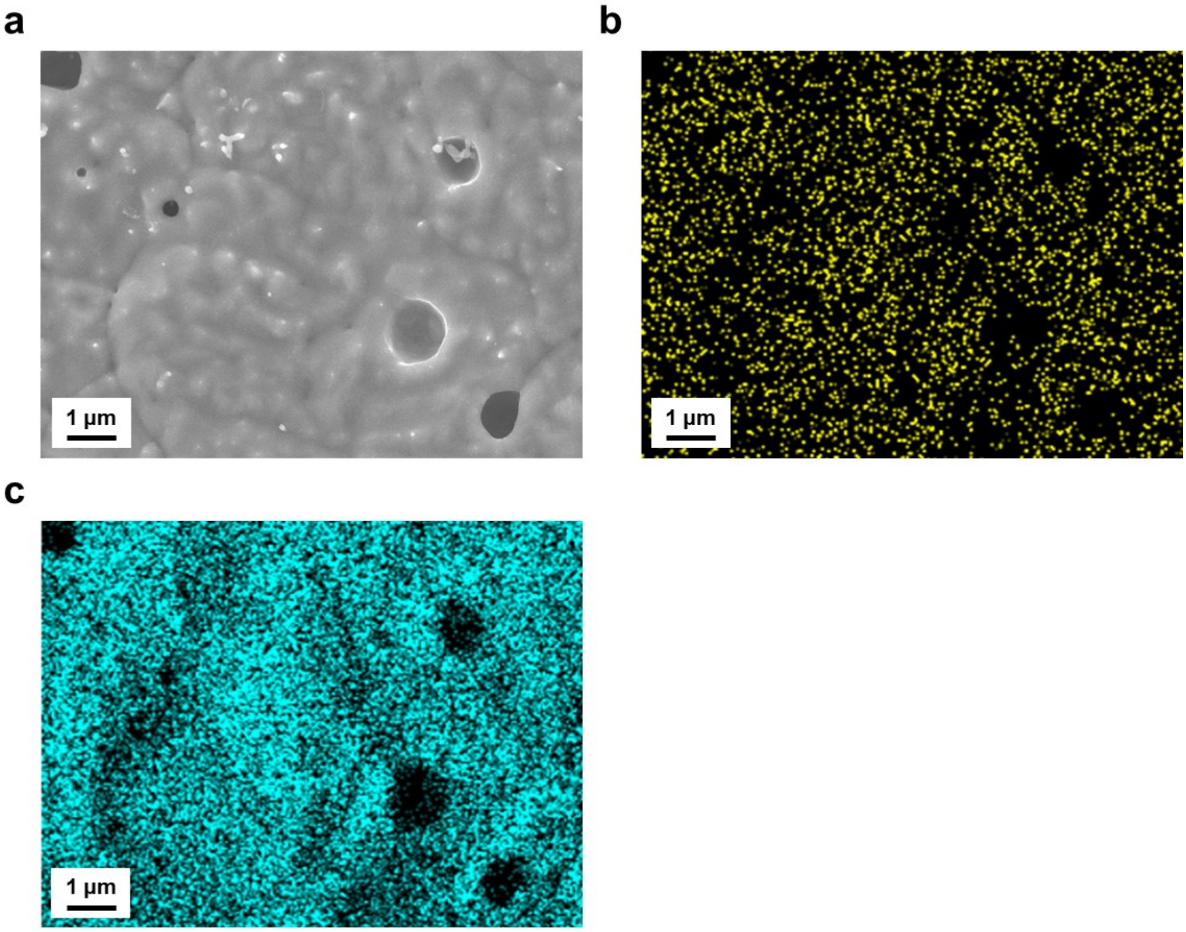

Figure S3. (a) FE-SEM image, and corresponding EDS elemental mapping of (b) Co and (c) Cu of Co-Cu/CF.

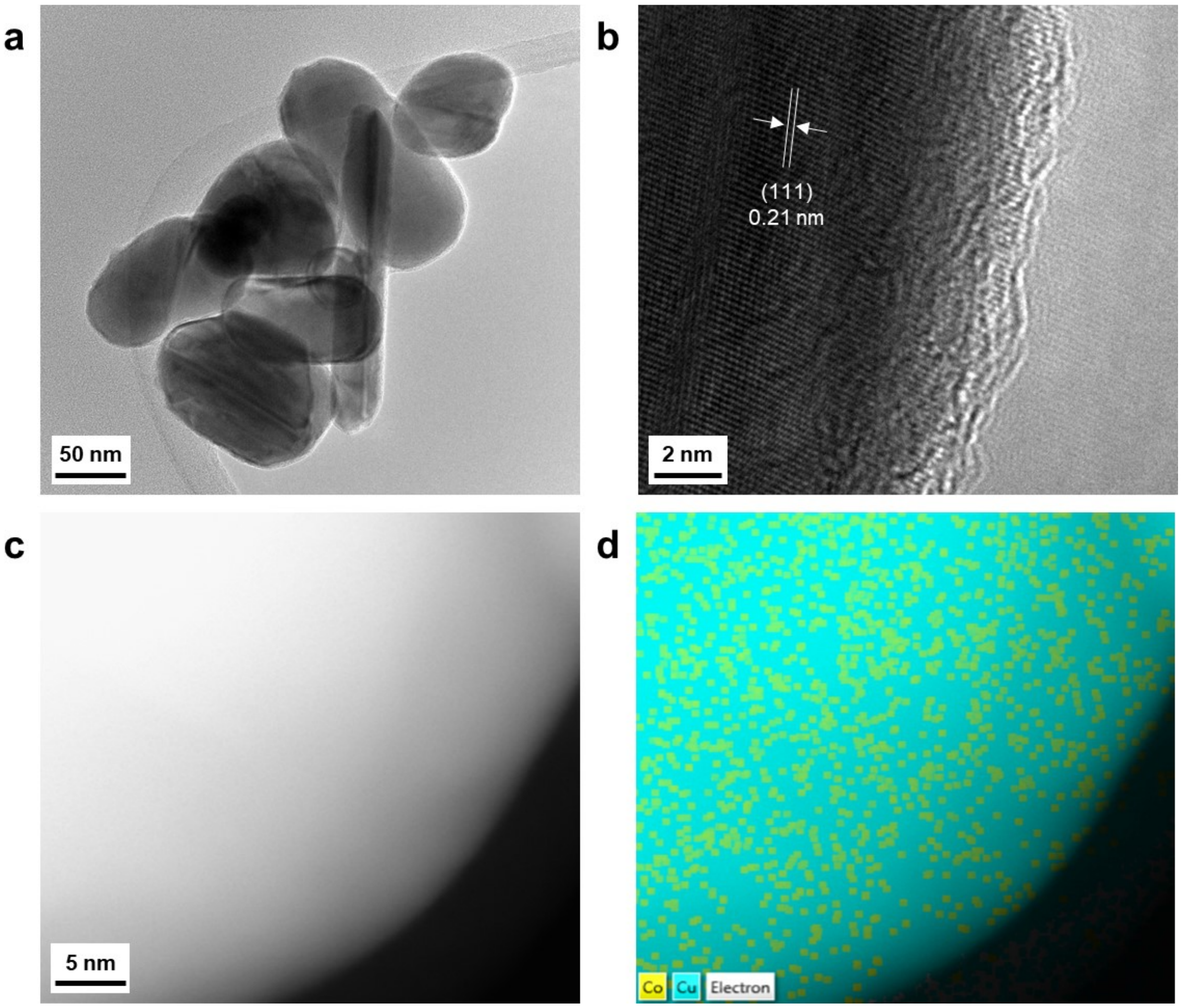

Figure S4. (a) TEM image, (b) HRTEM image, (c) HAADF-STEM image, and (d) corresponding EDS elemental mappings of Co-Cu/CF.

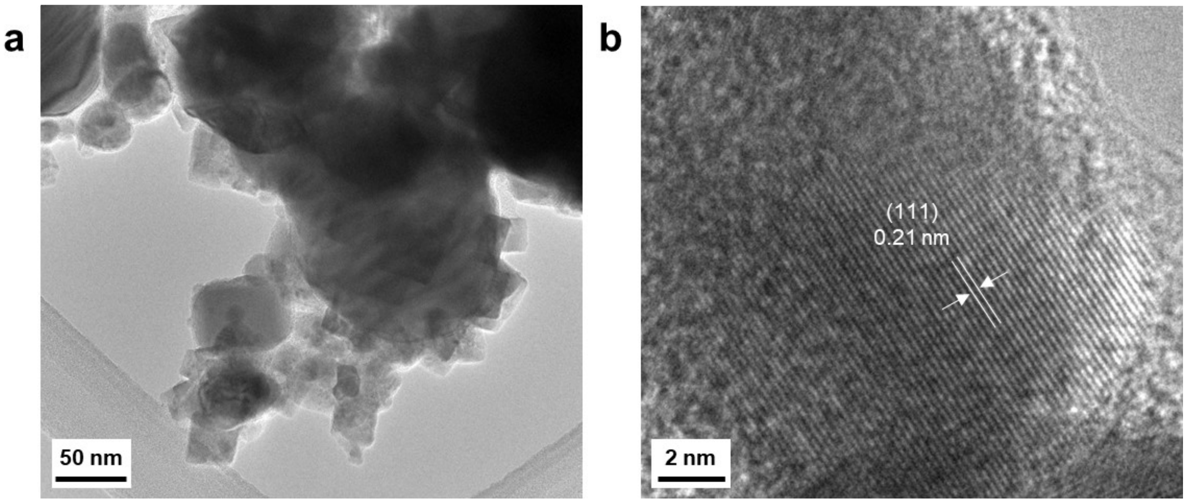

Figure S5. (a) TEM image, and (b) HRTEM image of Cu/CF.

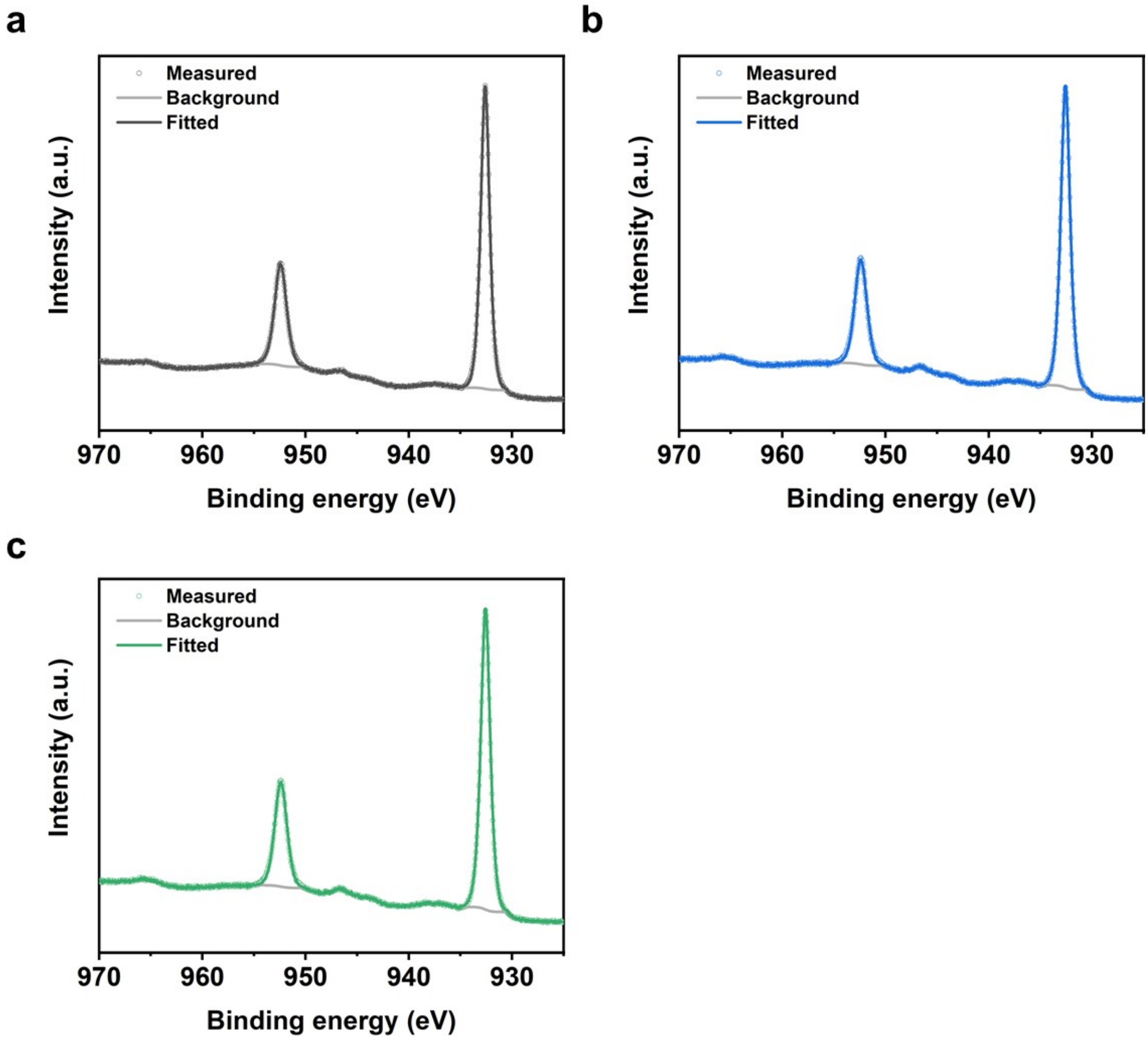

Figure S6. Cu 2p XPS spectra of (a) Co-Cu/CF, (b) Pt-Cu/CF, and (c) Cu/CF.

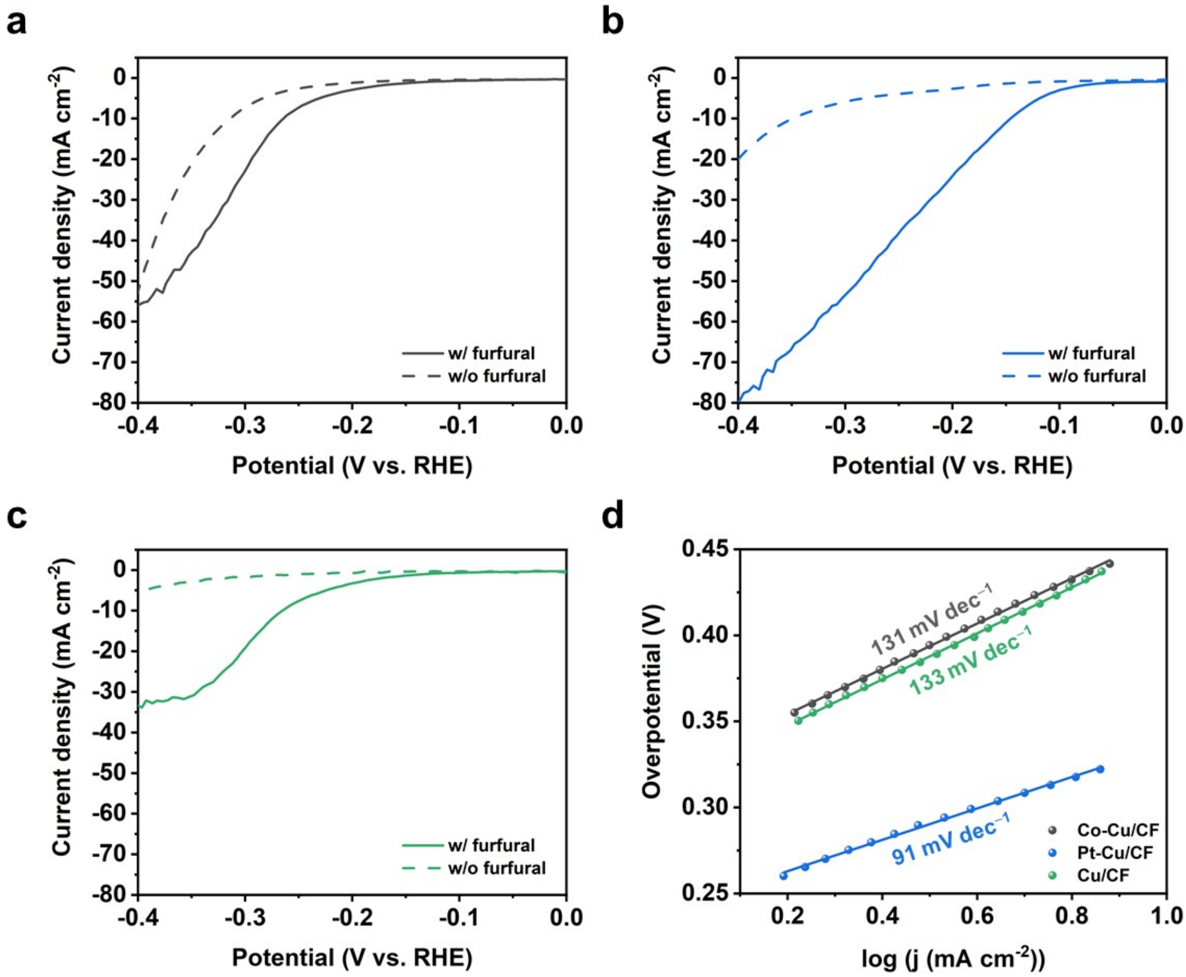

Figure S7. LSV curves of (a) Co-Cu/CF, (b) Pt-Cu/CF, and (c) Cu/CF recorded in the absence (dotted lines) and presence (solid lines) of 0.03 M FF. (d) Tafel slopes of the catalysts.

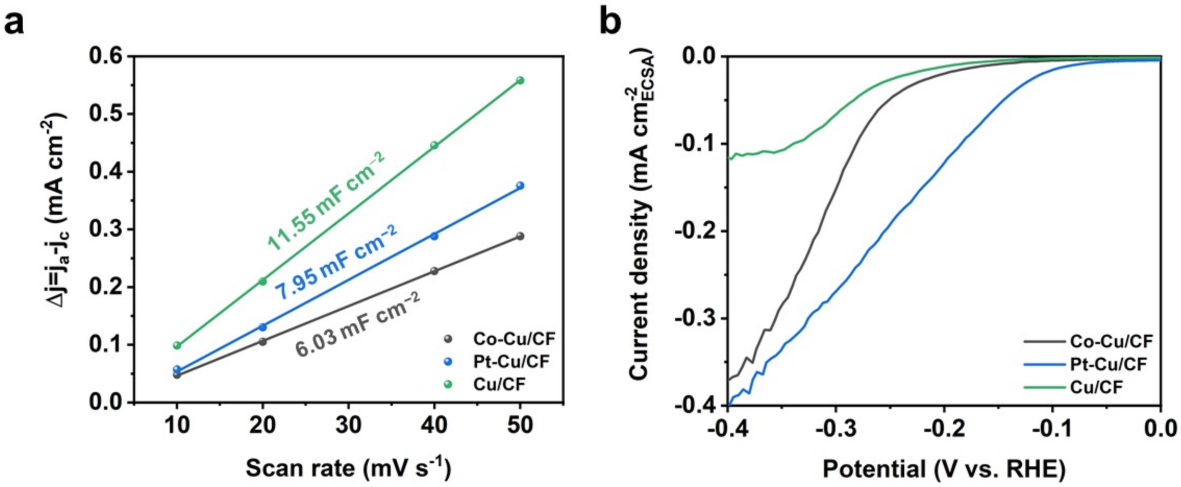

Figure S8. (a) C_{dl} measurements and (b) ECSA normalized current densities of Co-Cu/CF, Pt-Cu/CF, and Cu/CF.

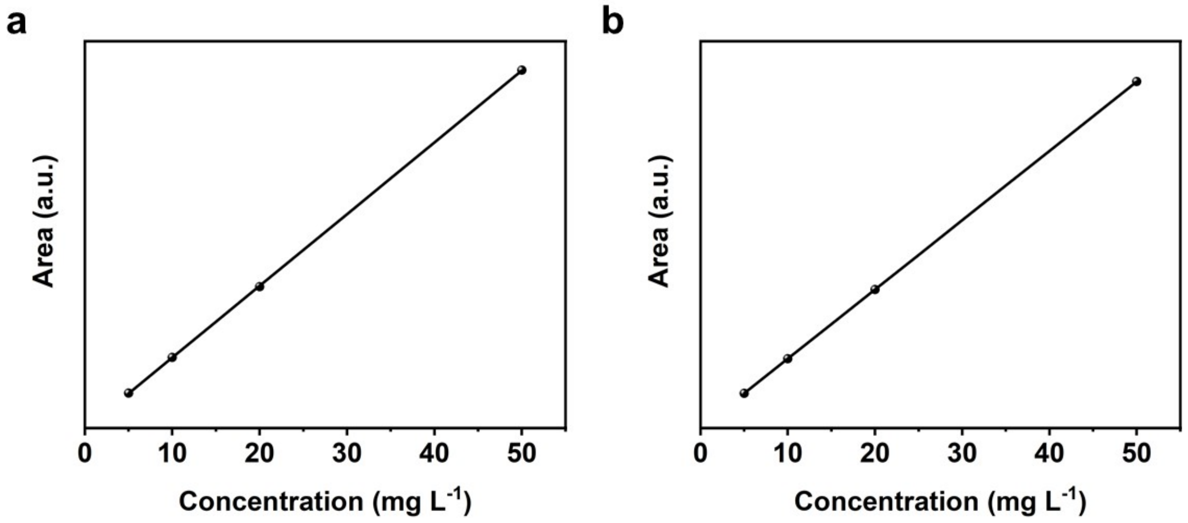

Figure S9. Calibration curves for quantitative analysis of (a) FF and (b) FA determined by HPLC.

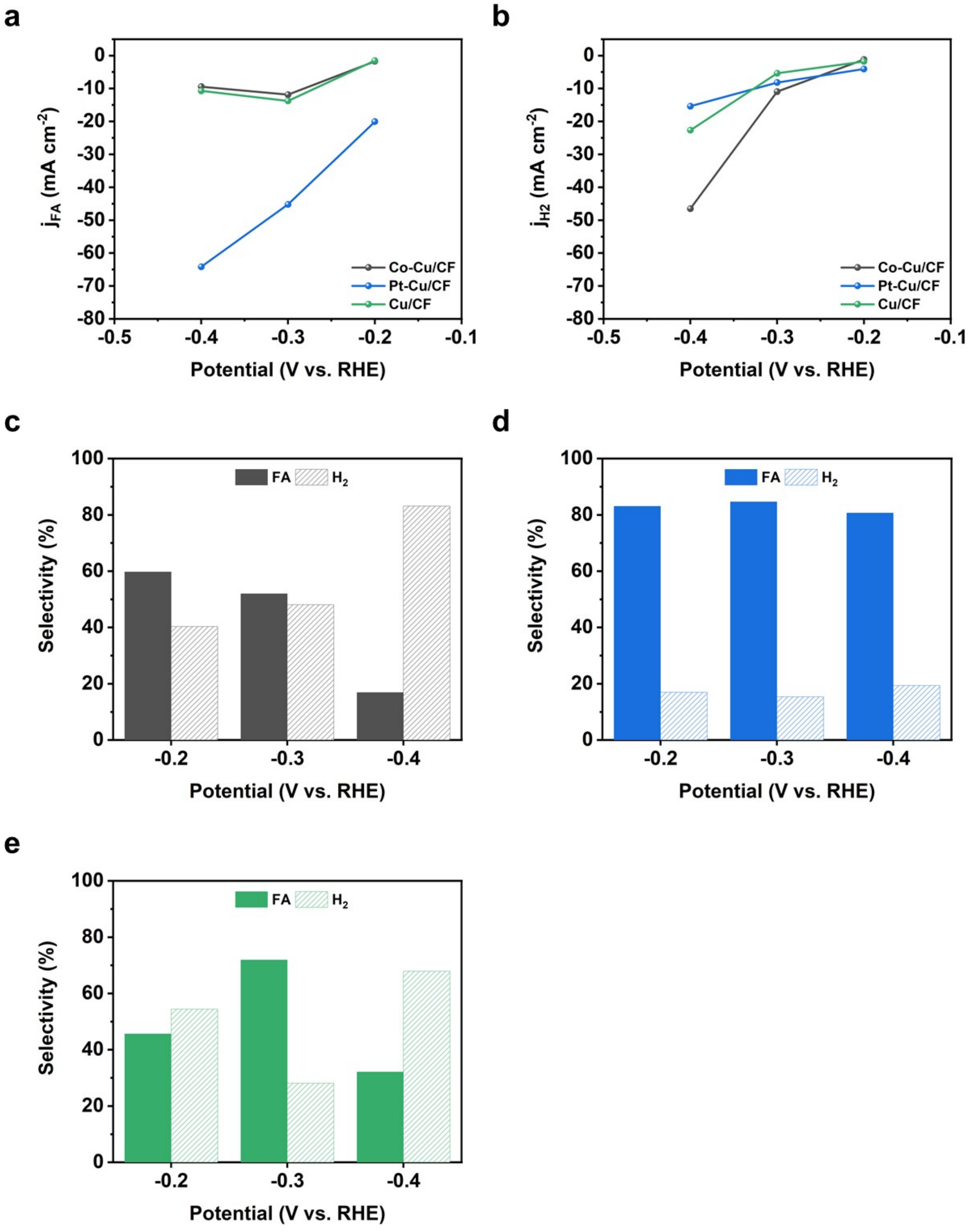

Figure S10. Partial current density toward (a) FA (j_{FA}) and (b) H_2 (j_{H2}) as a function of applied potential. Product selectivity of (c) Co-Cu/CF, (d) Pt-Cu/CF, and (e) Cu/CF.

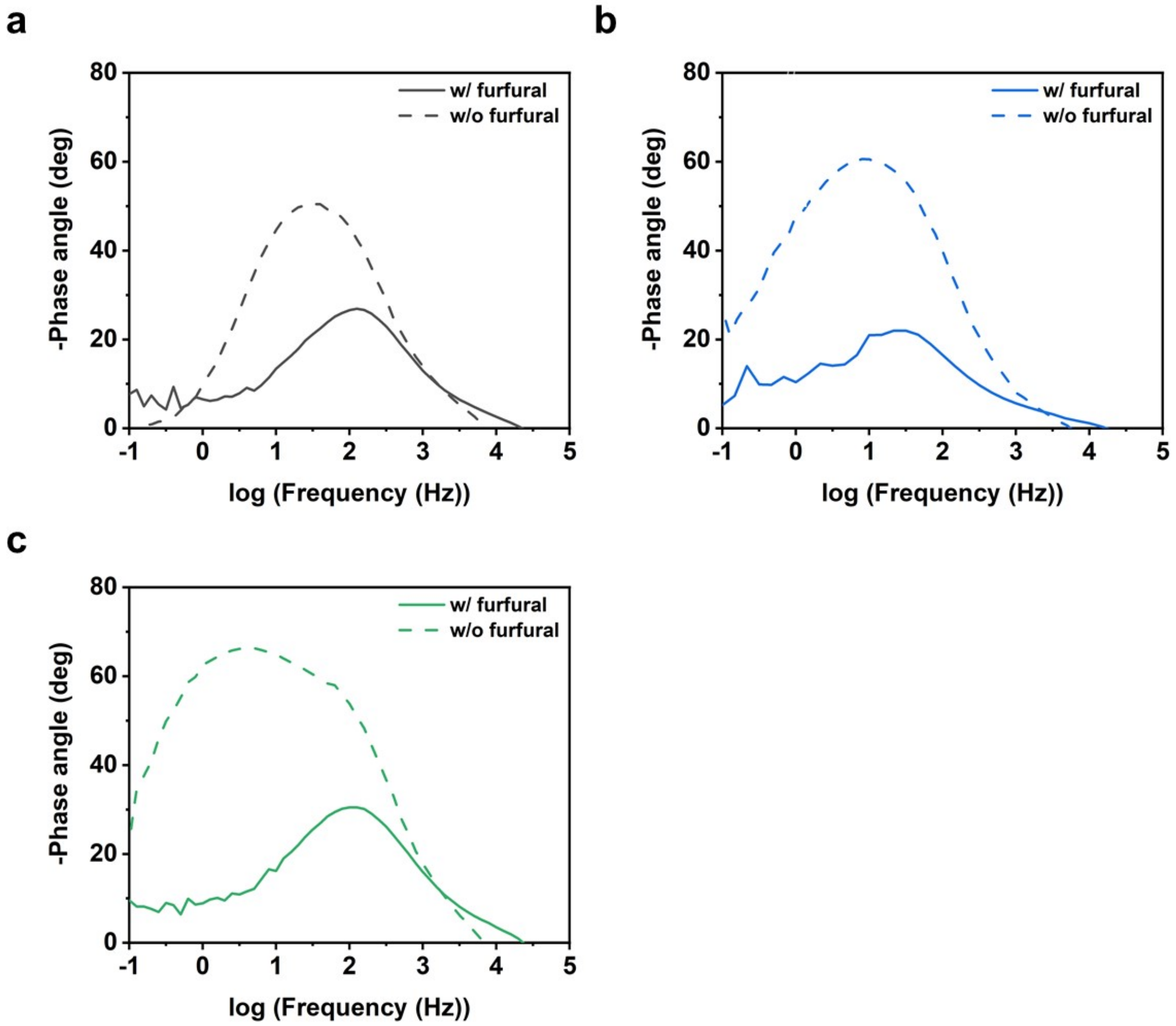

Figure S11. Bode plots of the (a) Co-Cu/CF, (b) Pt-Cu/CF, and (c) Cu/CF collected at -0.3 V with (solid line) and without (dotted line) 0.03 M FF.

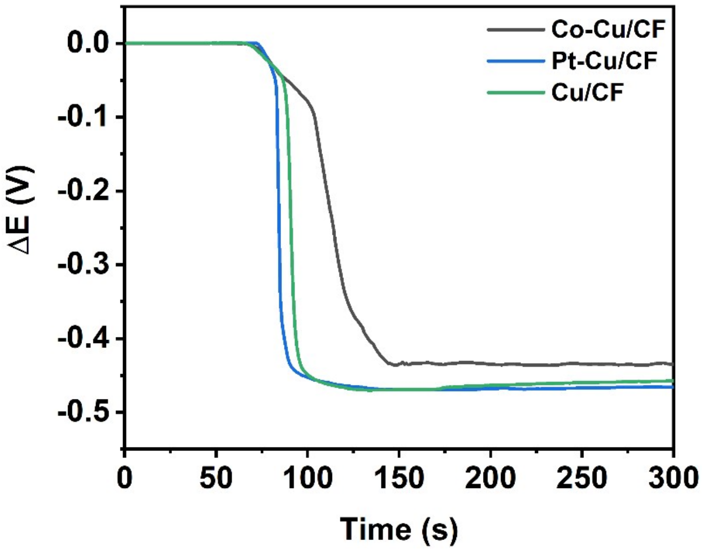

Figure S12. OCP changes of Co-Cu/CF, Pt-Cu/CF, and Cu/CF after FF addition.

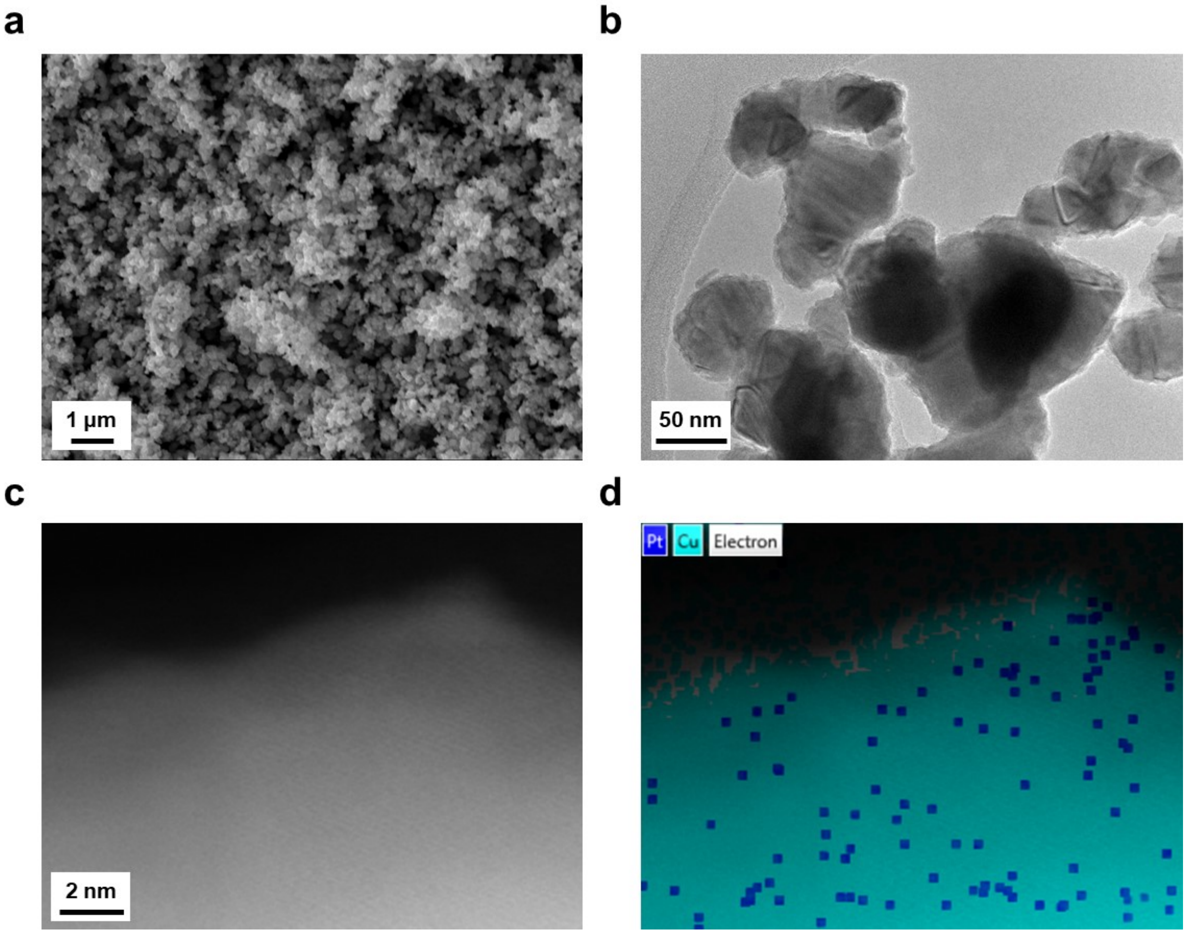

Figure S13. Ex-situ (a) SEM image, (b) TEM image, (c) HAADF-STEM image, and (d) corresponding EDS elemental mapping of Pt-Cu/CF after the stability test.

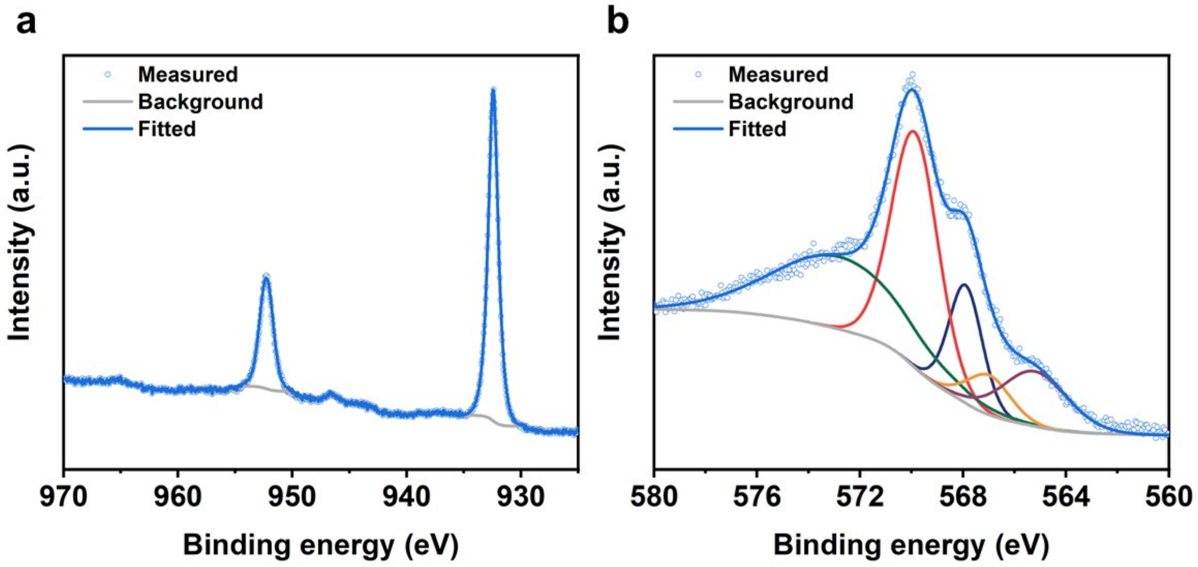

Figure S14. Ex-situ (a) Cu 2p and (b) Cu LMM XPS spectra of Pt-Cu/CF after the stability test.

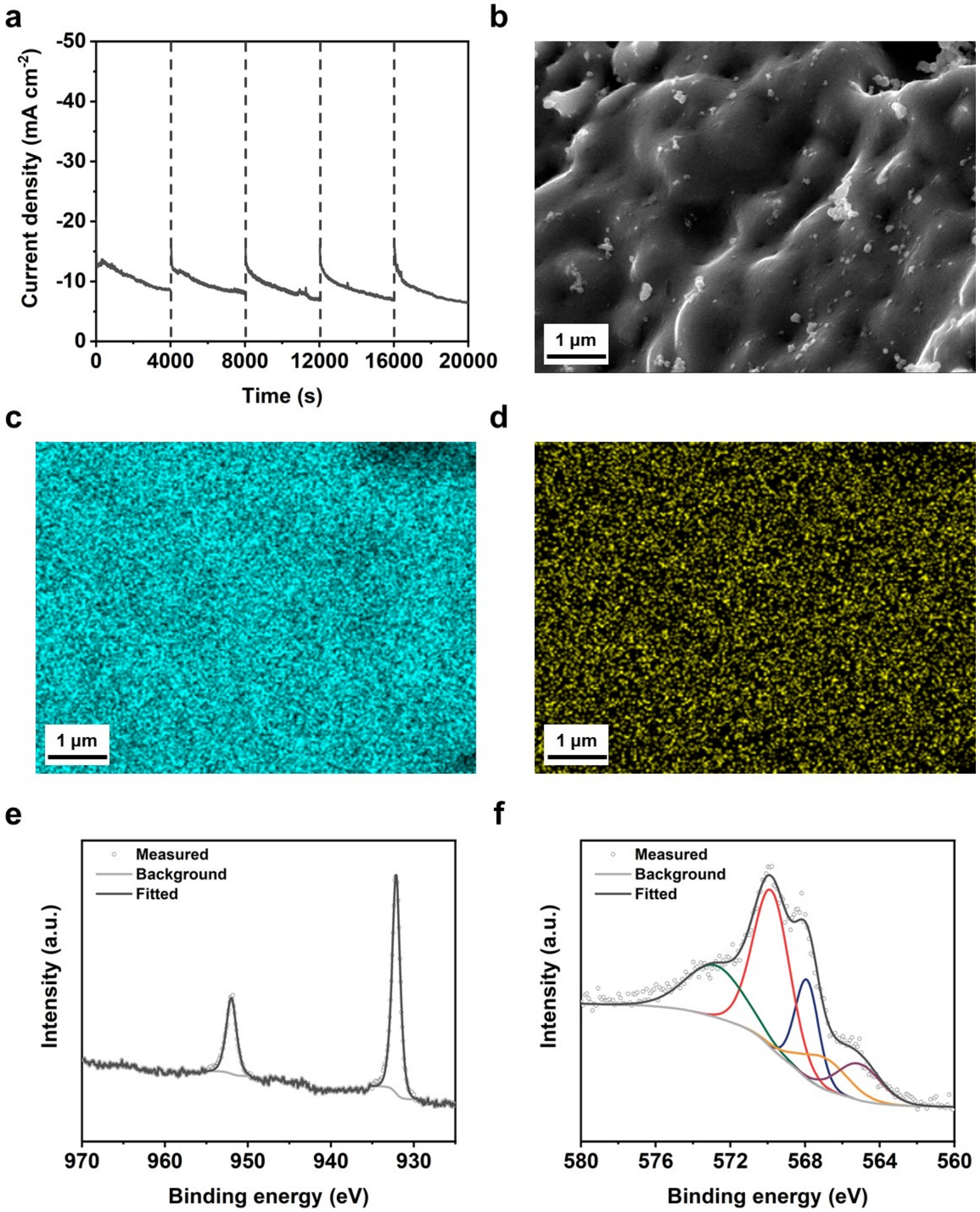

Figure S15. (a) CA stability test of Co-Cu/CF measured at −0.3 V in 1 M KOH containing 0.03 M FF. Ex-situ (b) FE-SEM image, and corresponding EDS elemental mapping of (c) Cu and (d) Co of Co-Cu/CF. Ex-situ (e) Cu 2p and (f) Cu LMM XPS spectra of Co-Cu/CF after the stability test.

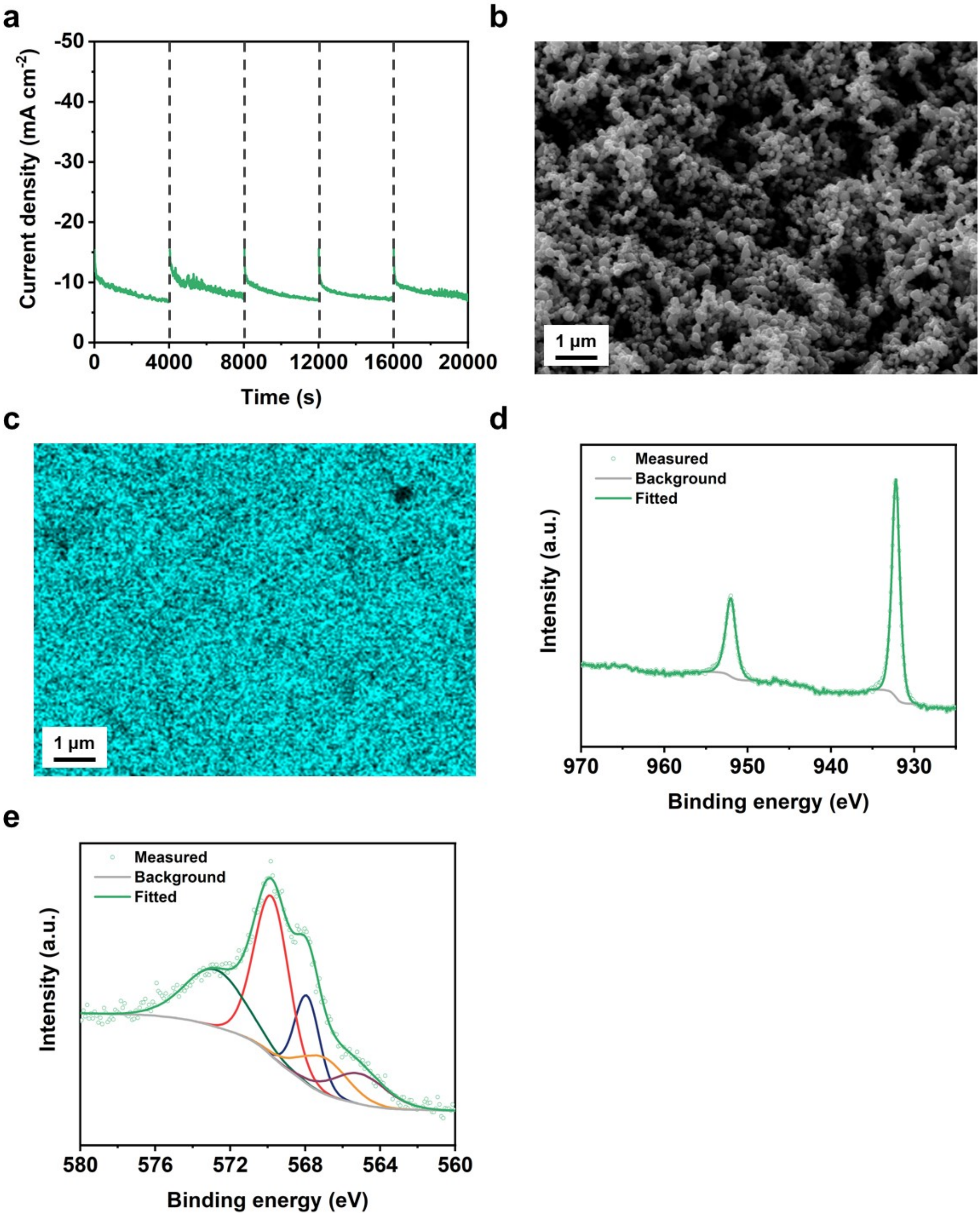

Figure S16. (a) CA stability test of Cu/CF measured at −0.3 V in 1 M KOH containing 0.03 M FF. Ex-situ (b) FE-SEM images, and corresponding EDS elemental mapping of (c) Cu of Cu/CF. Ex-situ (d) Cu 2p and (e) Cu LMM XPS spectra of Cu/CF after the stability test.

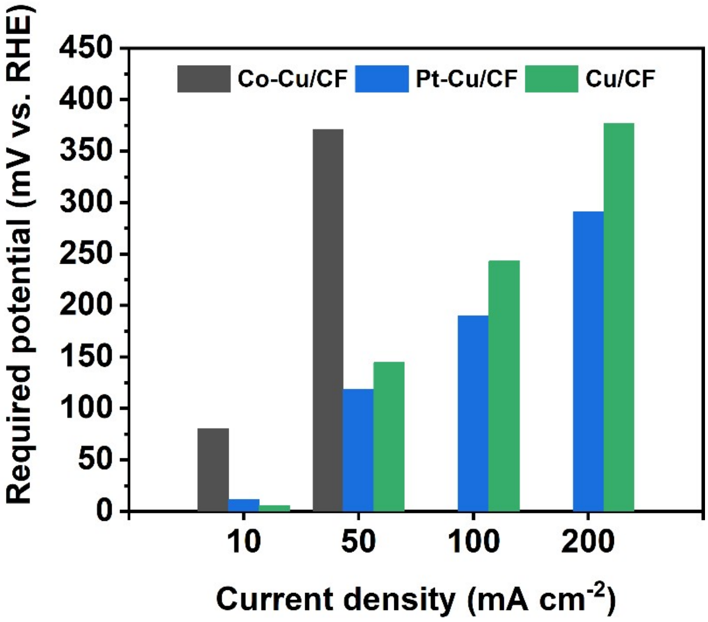

Figure S17. Required potentials to achieve current densities of 10, 50, 100, and 200 mA cm^{-2} for Co-Cu/CF, Pt-Cu/CF, and Cu/CF.

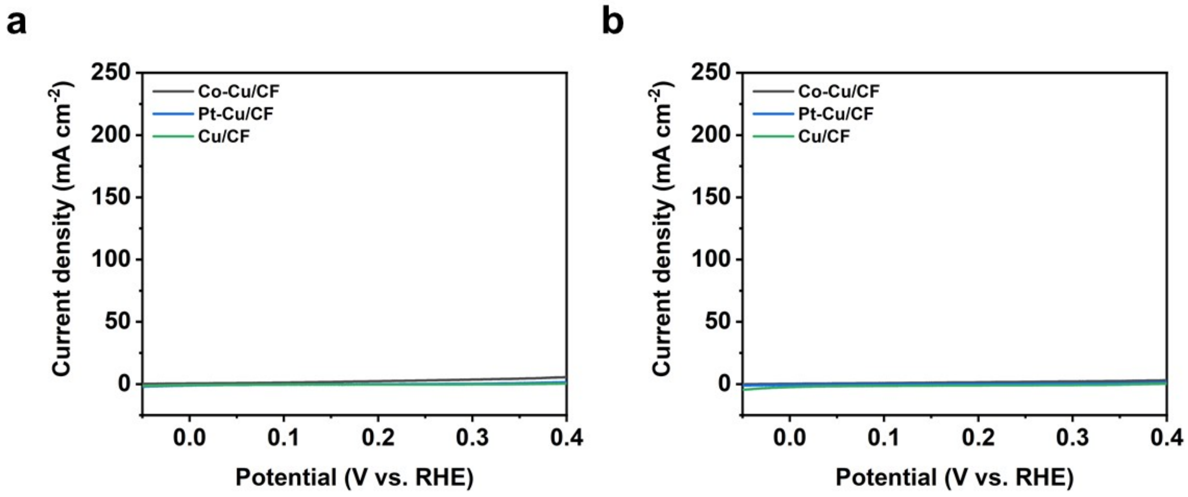

Figure S18. LSV curves of Co-Cu/CF, Pt-Cu/CF, and Cu/CF acquired with (a) 0.6 M CH_3OH and (b) 0.6 M HCOOK.

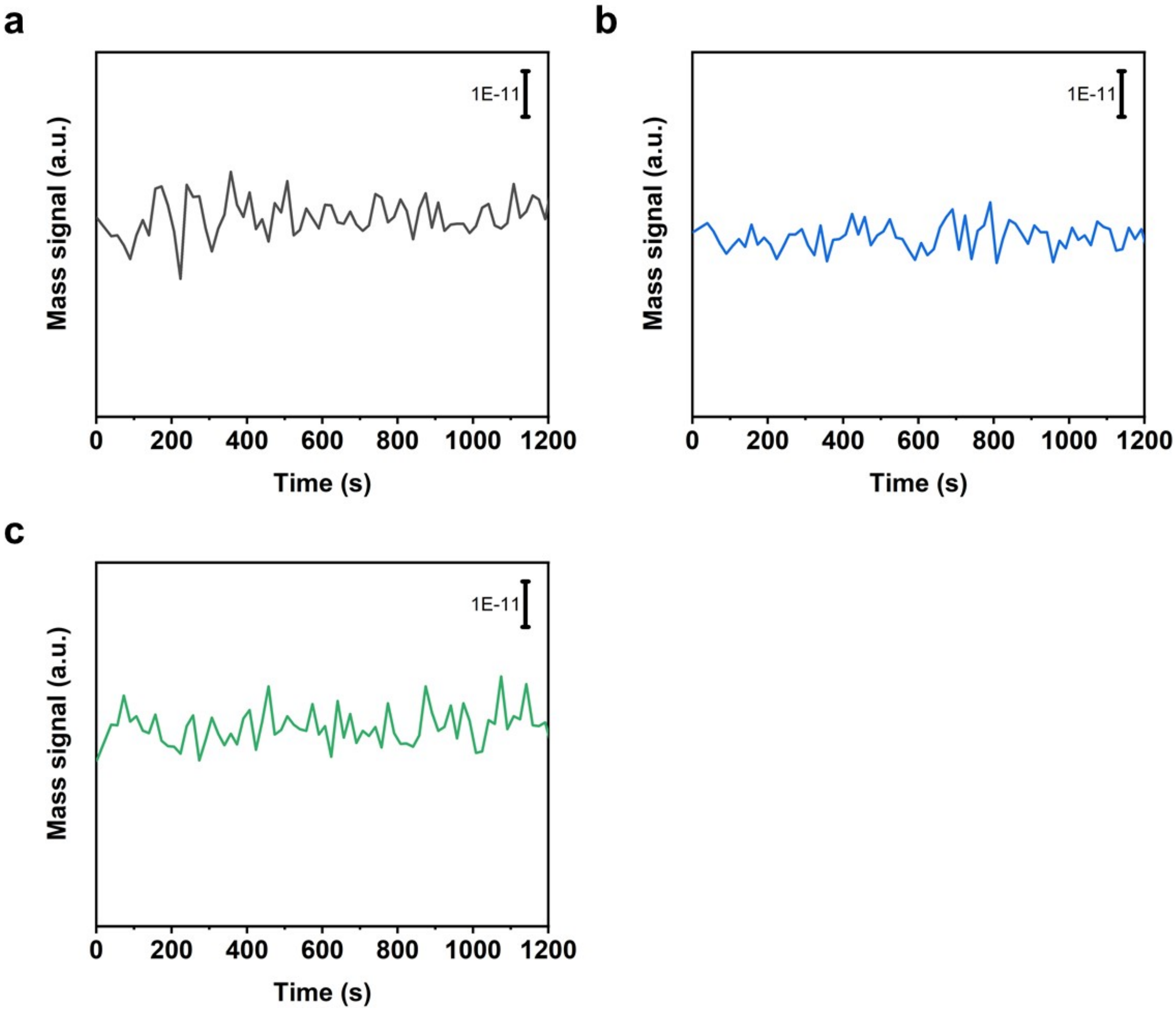

Figure S19. OLEMS results monitoring the m/z = 44 signal (CO_2) during the FOR over (a) Co-Cu/CF, (b) Pt-Cu/CF, and (c) Cu/CF.

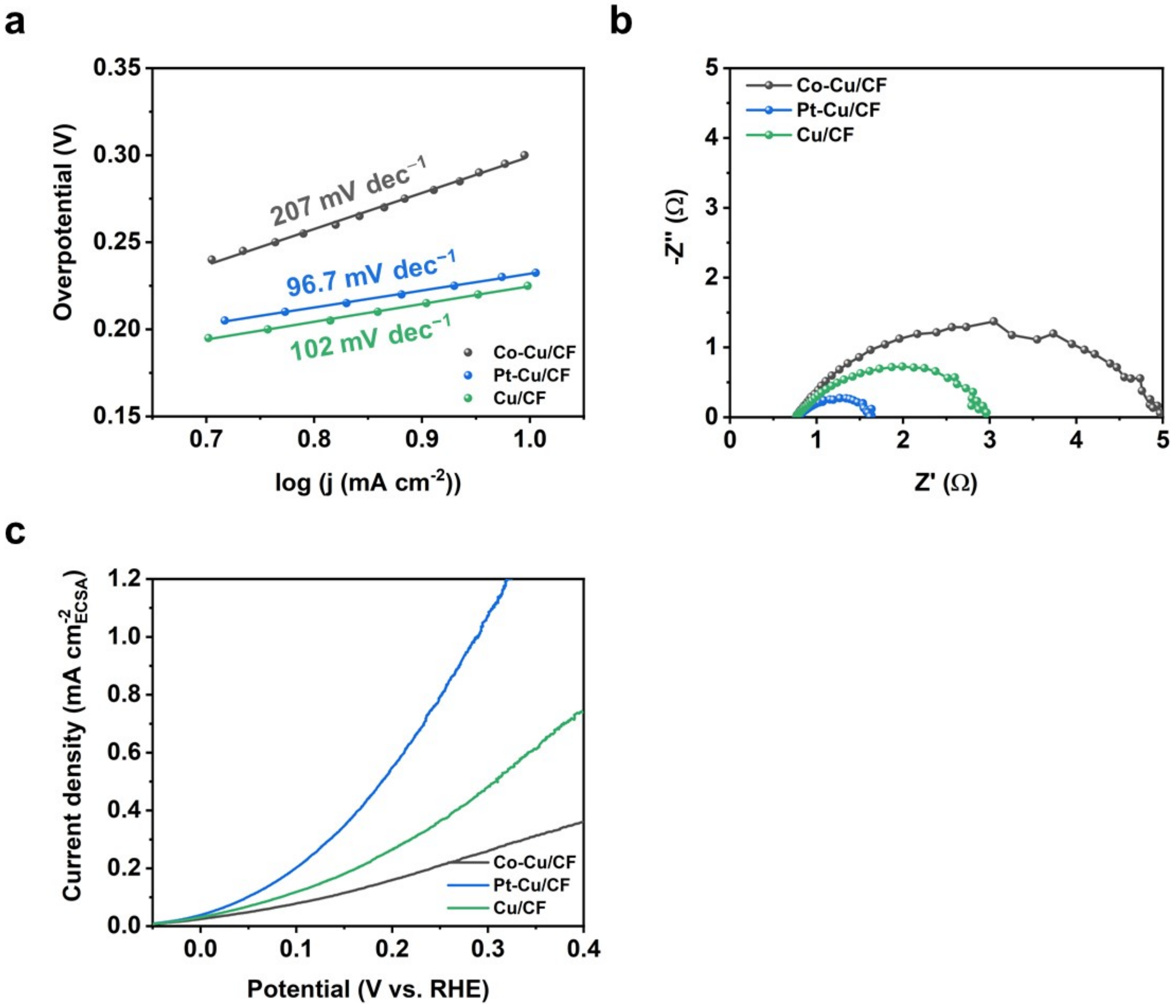

Figure S20. (a) Tafel slopes, (b) Nyquist plots measured at 0.3 V, and (c) ECSA normalized current densities of Co-Cu/CF, Pt-Cu/CF, and Cu/CF.

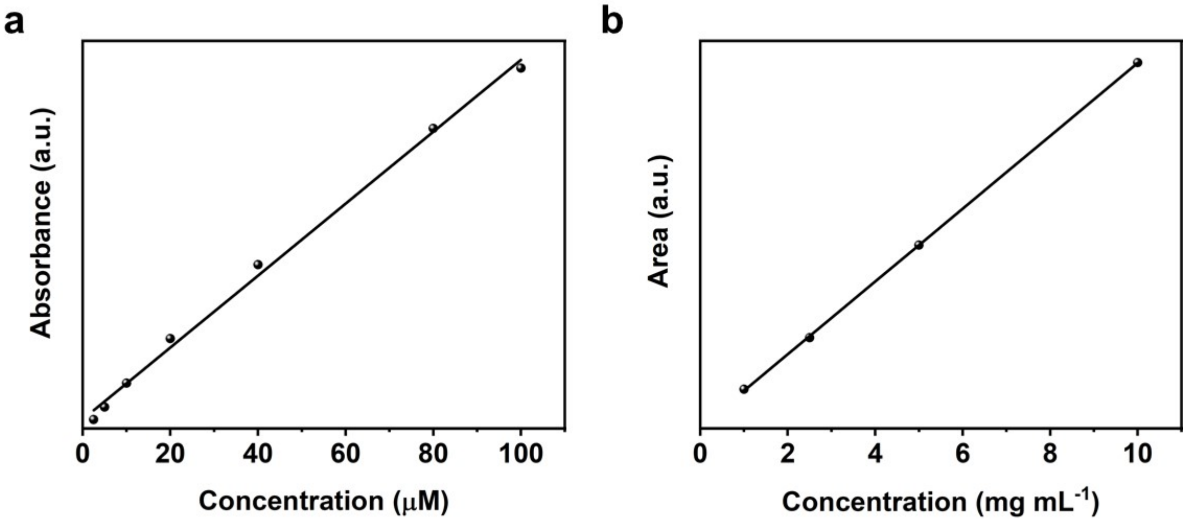

Figure S21. Calibration curves for quantitative analysis of (a) HCHO obtained from UV–Vis spectroscopy and (b) HCOOH determined by HPLC.

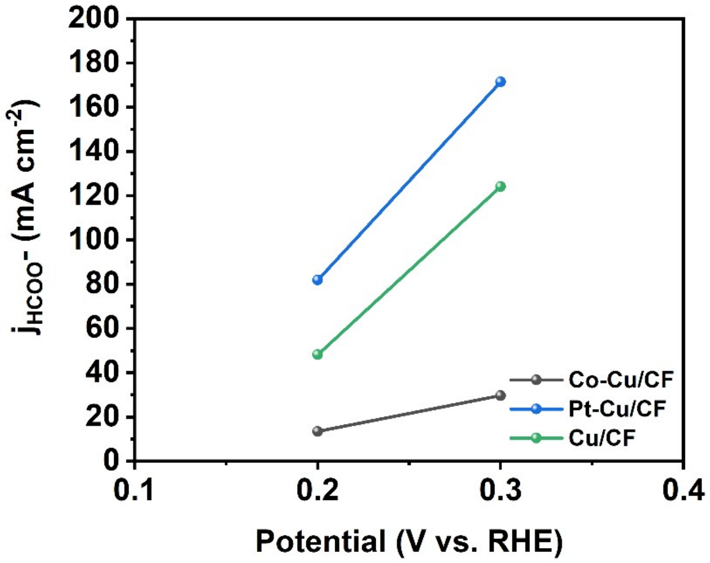

Figure S22. Partial current density toward $HCOO^-$ (j_{HCOO^-}) as a function of applied potential.

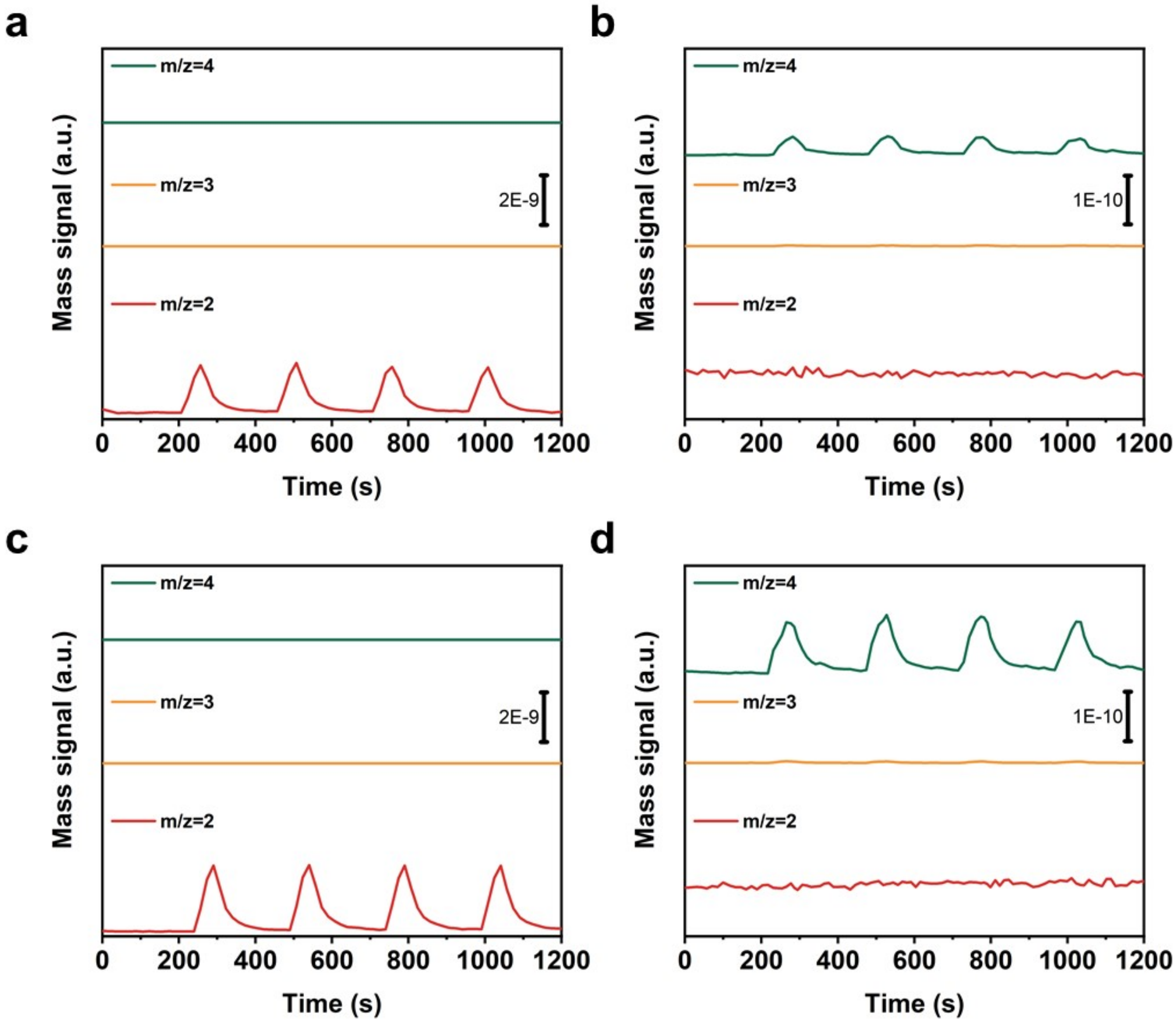

Figure S23. OLEMS results of Co-Cu/CF in 1 M KOH containing (a) HCHO and (b) DCDO. OLEMS results of Cu/CF in 1 M KOH containing (c) HCHO and (d) DCDO.

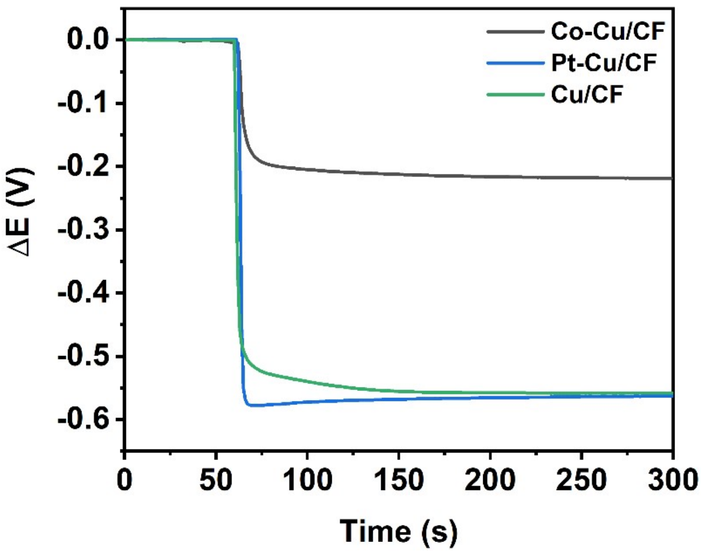

Figure S24. OCP changes of Co-Cu/CF, Pt-Cu/CF, and Cu/CF after HCHO addition.

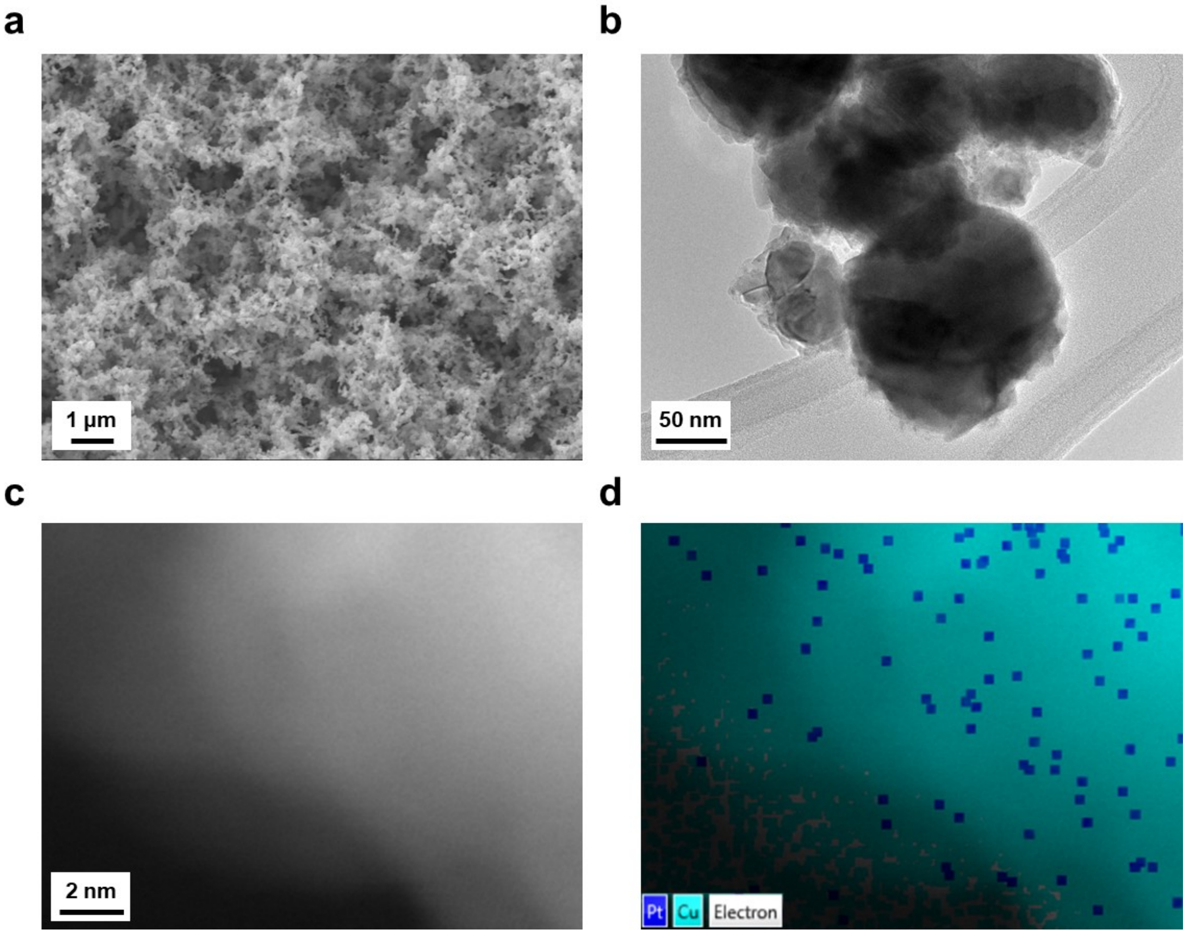

Figure S25. Ex-situ (a) SEM image, (b) TEM image, (c) HAADF-STEM image, and (d) corresponding EDS elemental mapping of Pt-Cu/CF after the stability test.

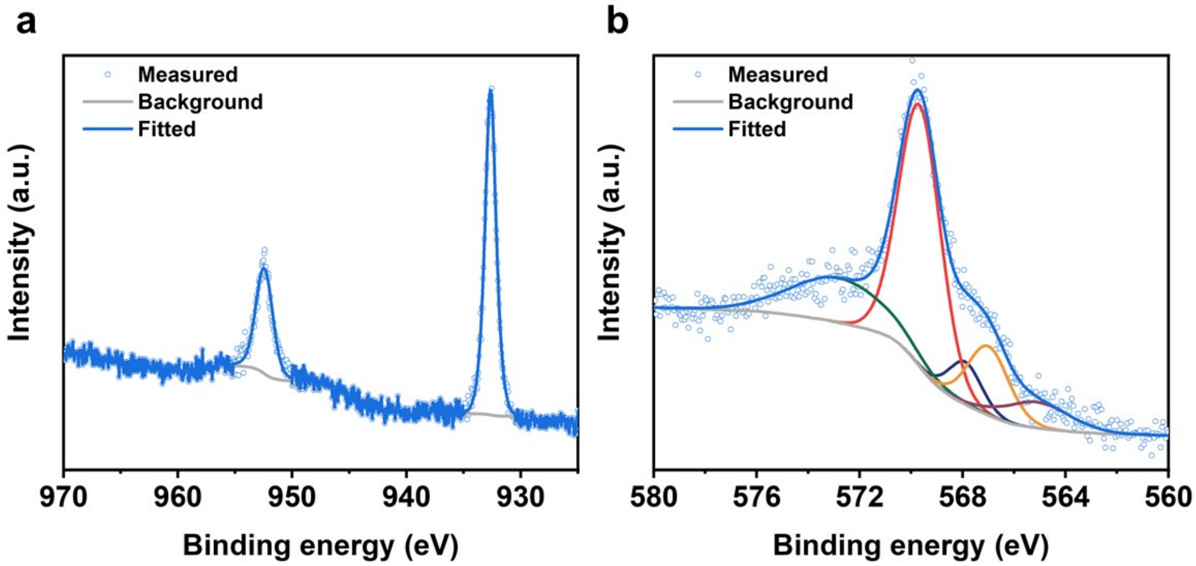

Figure S26. Ex-situ (a) Cu 2p and (b) Cu LMM XPS spectra of Pt-Cu/CF after the stability test.

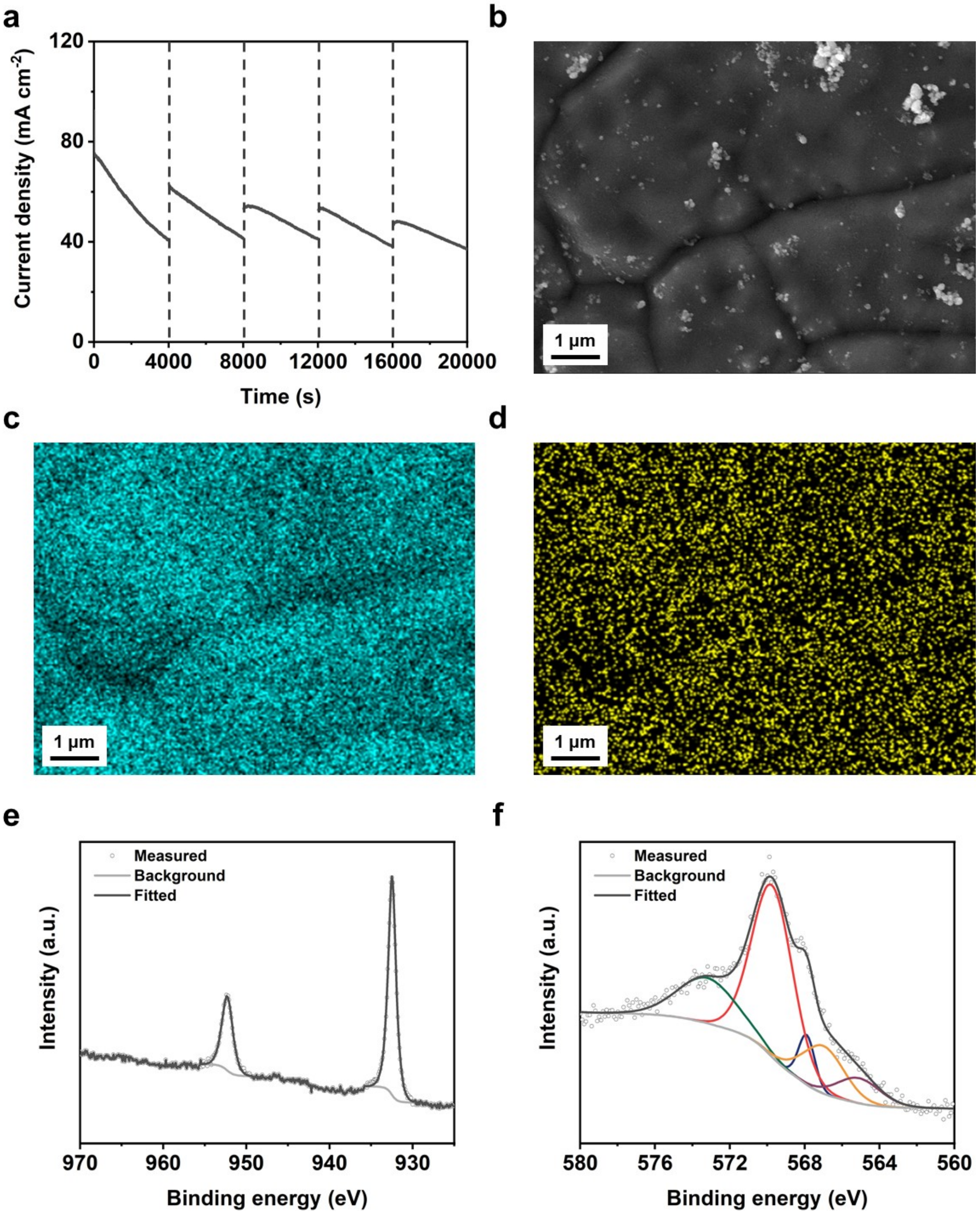

Figure S27. (a) CA stability test of Co-Cu/CF measured at −0.3 V in 1 M KOH containing 0.6 M HCHO. Ex-situ (b) FE-SEM image, and corresponding EDS elemental mapping of (c) Cu and (d) Co of Co-Cu/CF. Ex-situ (e) Cu 2p and (f) Cu LMM XPS spectra of Co-Cu/CF after the stability test.

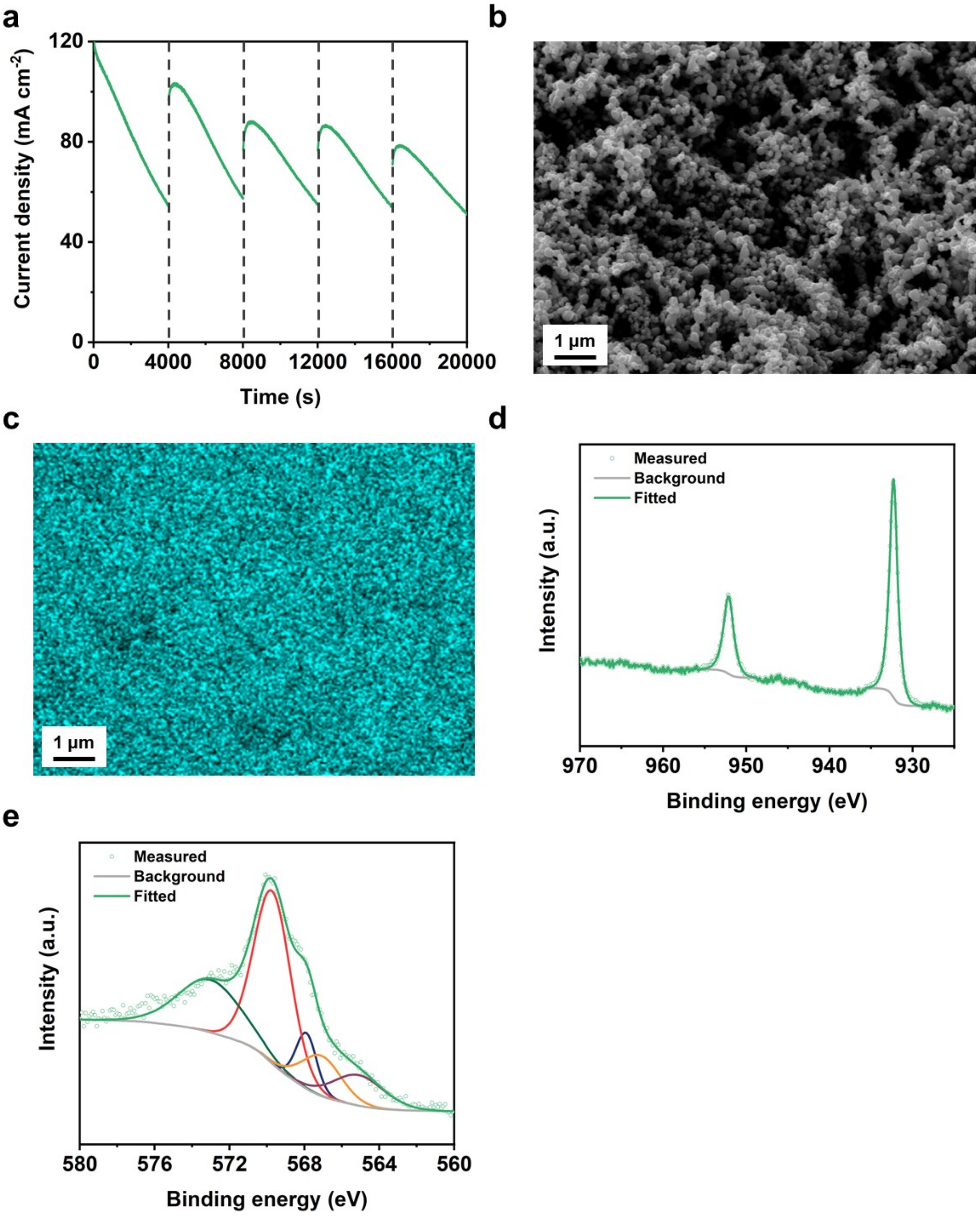

Figure S28. (a) CA stability test of Cu/CF measured at −0.3 V in 1 M KOH containing 0.6 M HCHO. Ex-situ (b) FE-SEM images, and corresponding EDS elemental mapping of (c) Cu of Cu/CF. Ex-situ (d) Cu 2p and (e) Cu LMM XPS spectra of Cu/CF after the stability test.

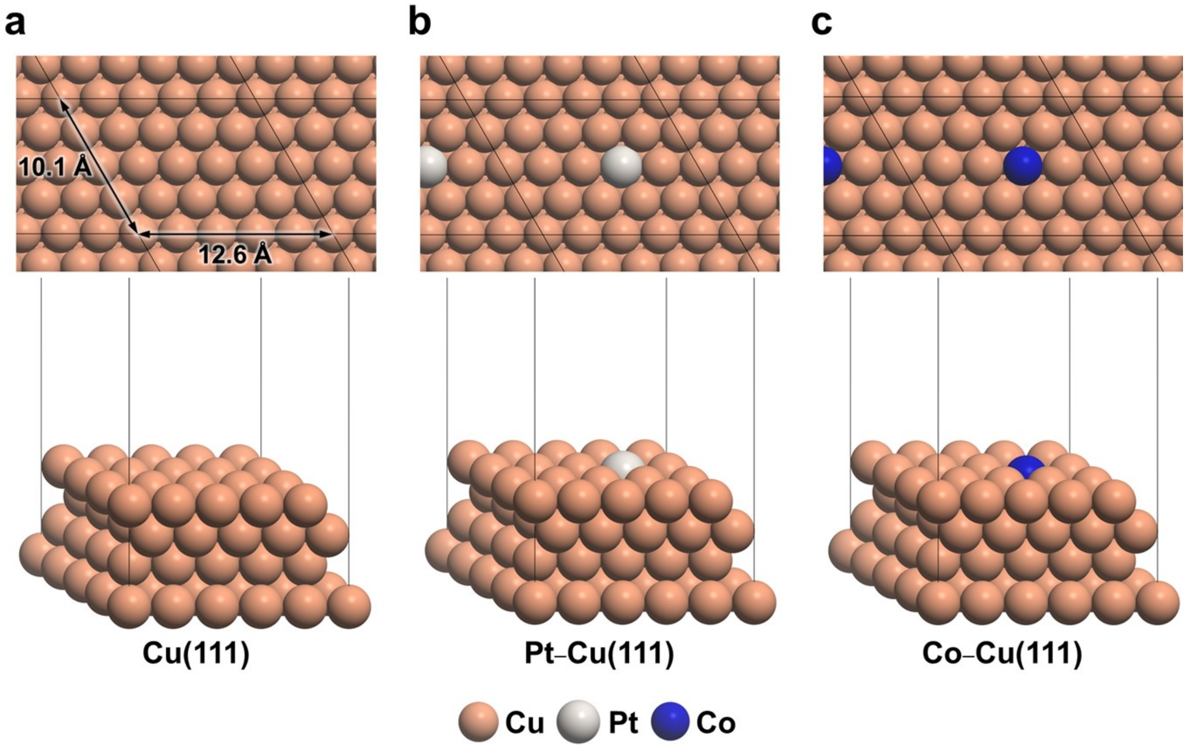

Figure S29. Optimized geometric structures (top and side views) of the computational slab models used for DFT calculations: (a) pristine Cu (111), (b) Pt-Cu (111), and (c) Co-Cu (111).

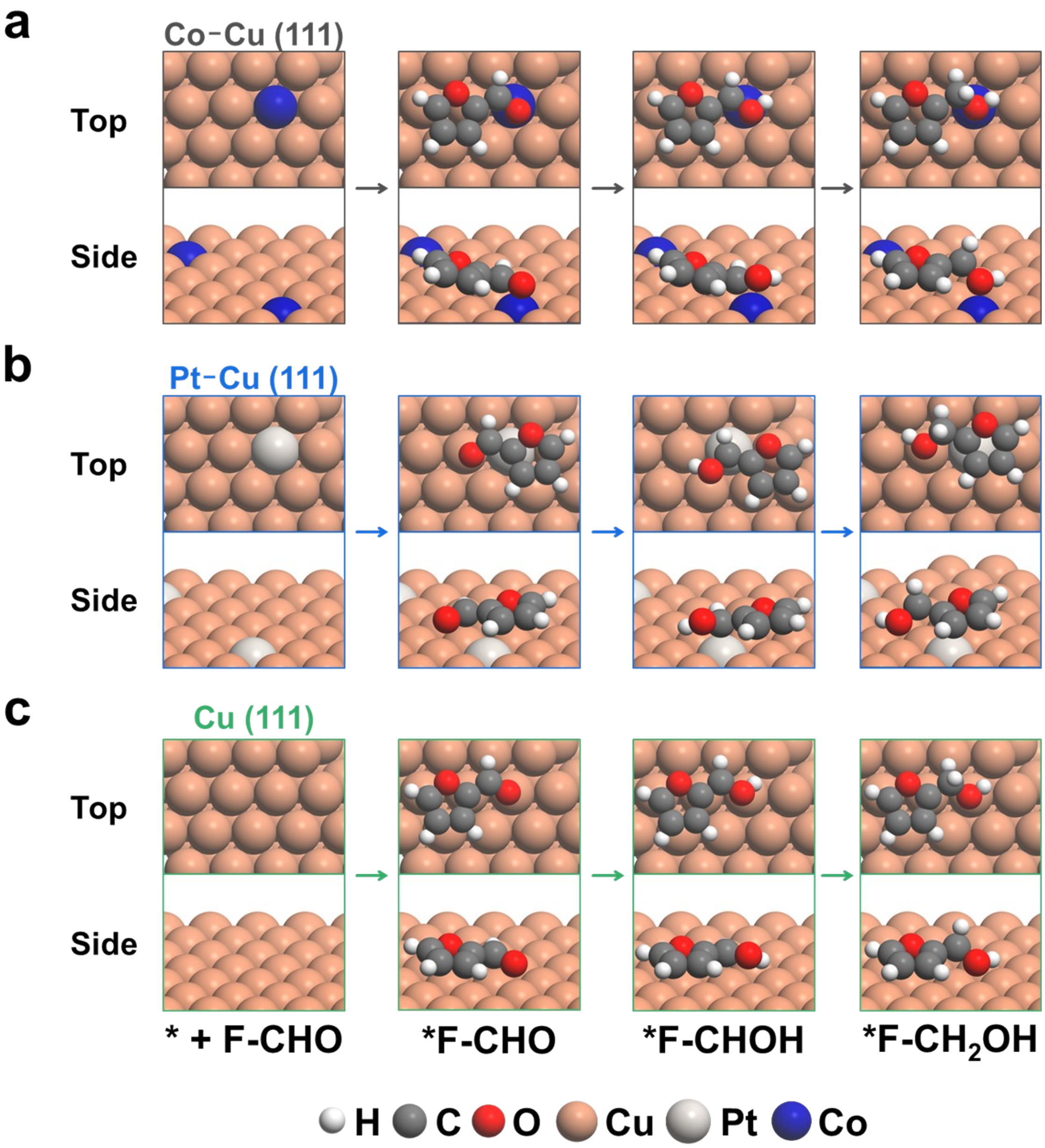

Figure S30. Optimized atomic configurations (top and side views) of the adsorbed intermediates and final states along the FEH pathway on (a) Co-Cu (111), (b) Pt-Cu (111), and (c) pristine Cu (111) surfaces.

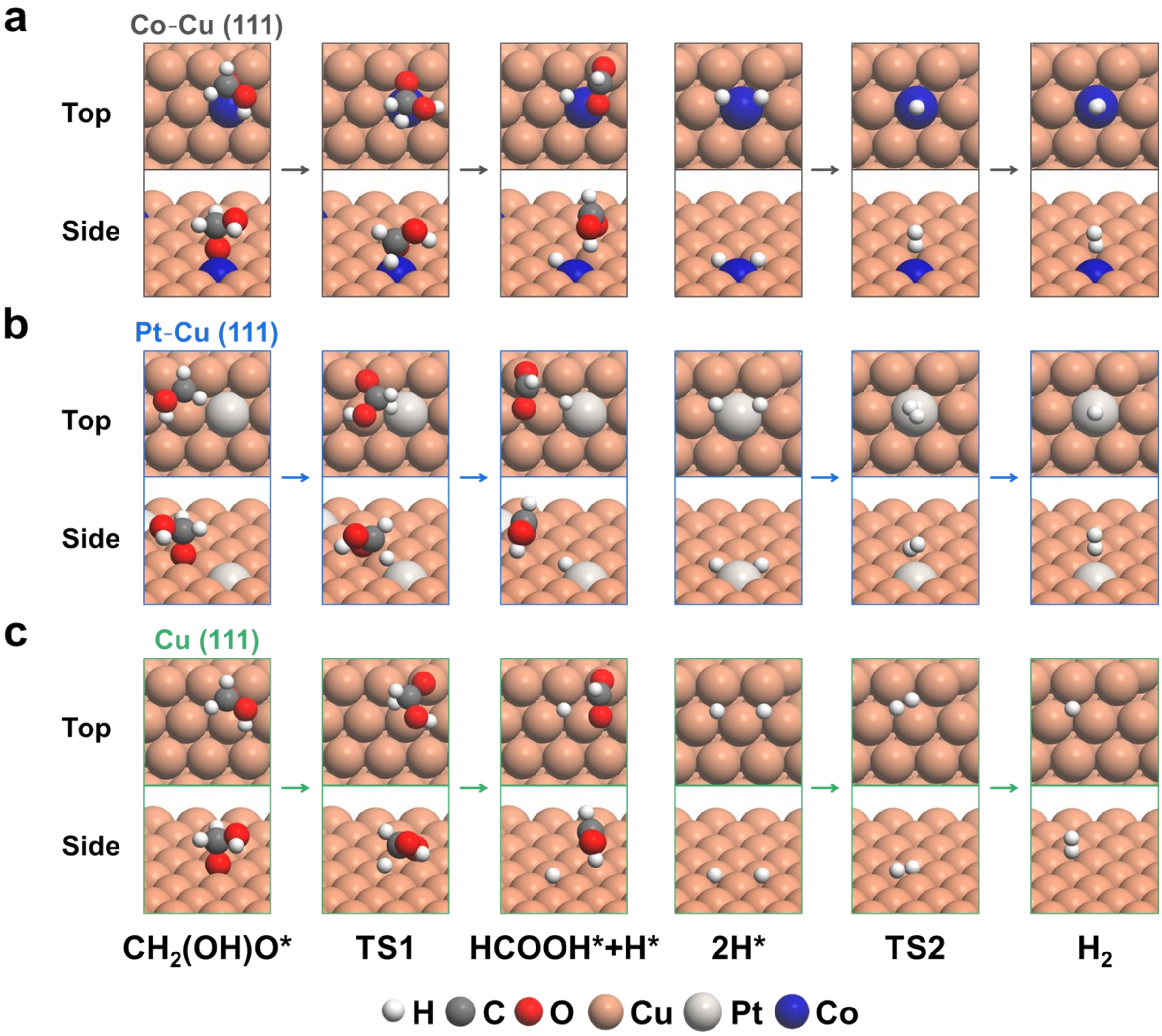

Figure S31. Optimized atomic configurations (top and side views) of the adsorbed intermediates and transition states along the formaldehyde oxidation pathway coupled with hydrogen recombination on (a) Co-Cu (111), (b) Pt-Cu (111), and (c) pristine Cu (111) surfaces.

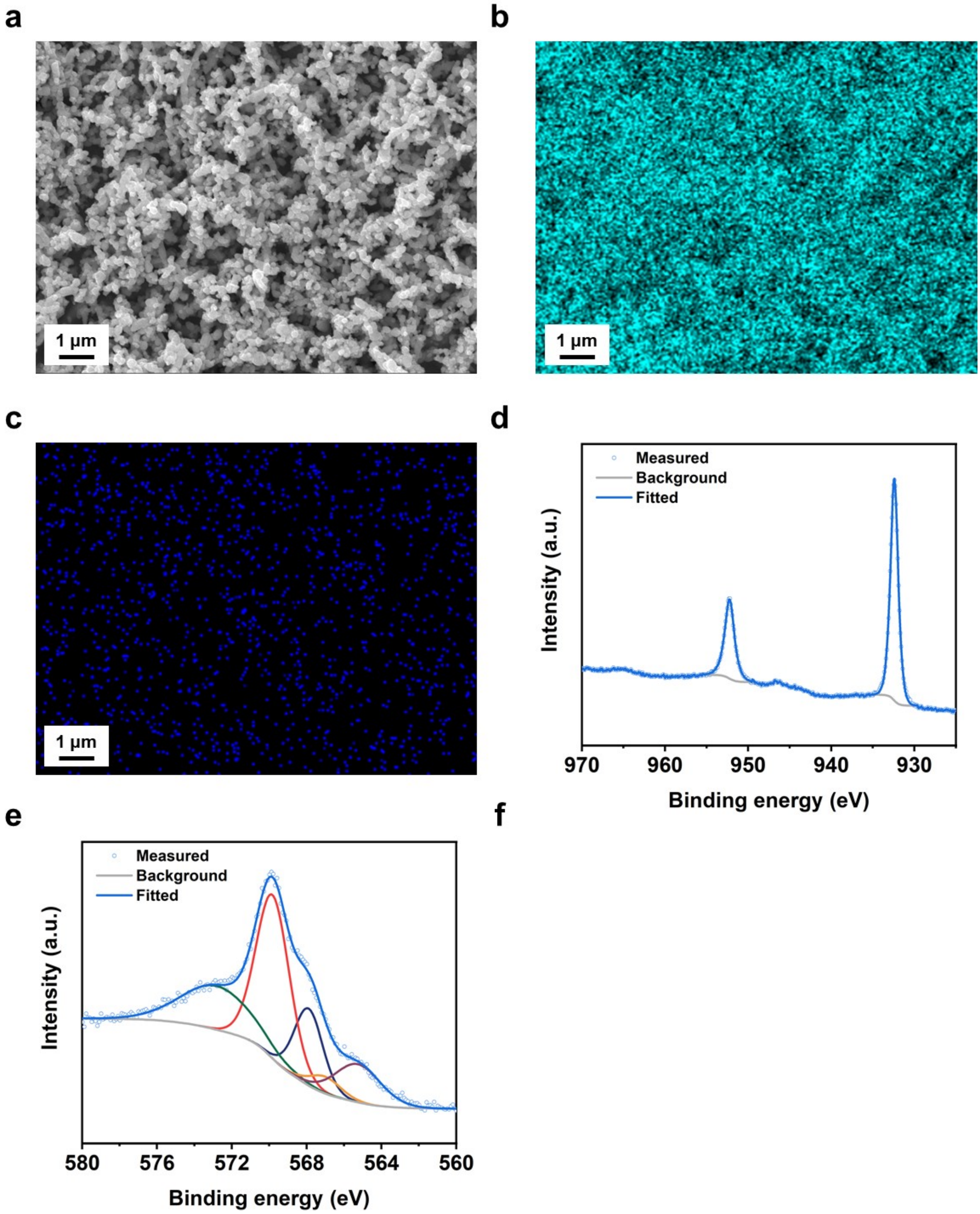

Figure S32. Ex-situ (a) FE-SEM image, and corresponding EDS elemental mapping of (b) Cu and (c) Pt of Pt-Cu/CF. Ex-situ (e) Cu 2p and (f) Cu LMM XPS spectra of Pt-Cu/CF after the stability test, all obtained from the cathode side.

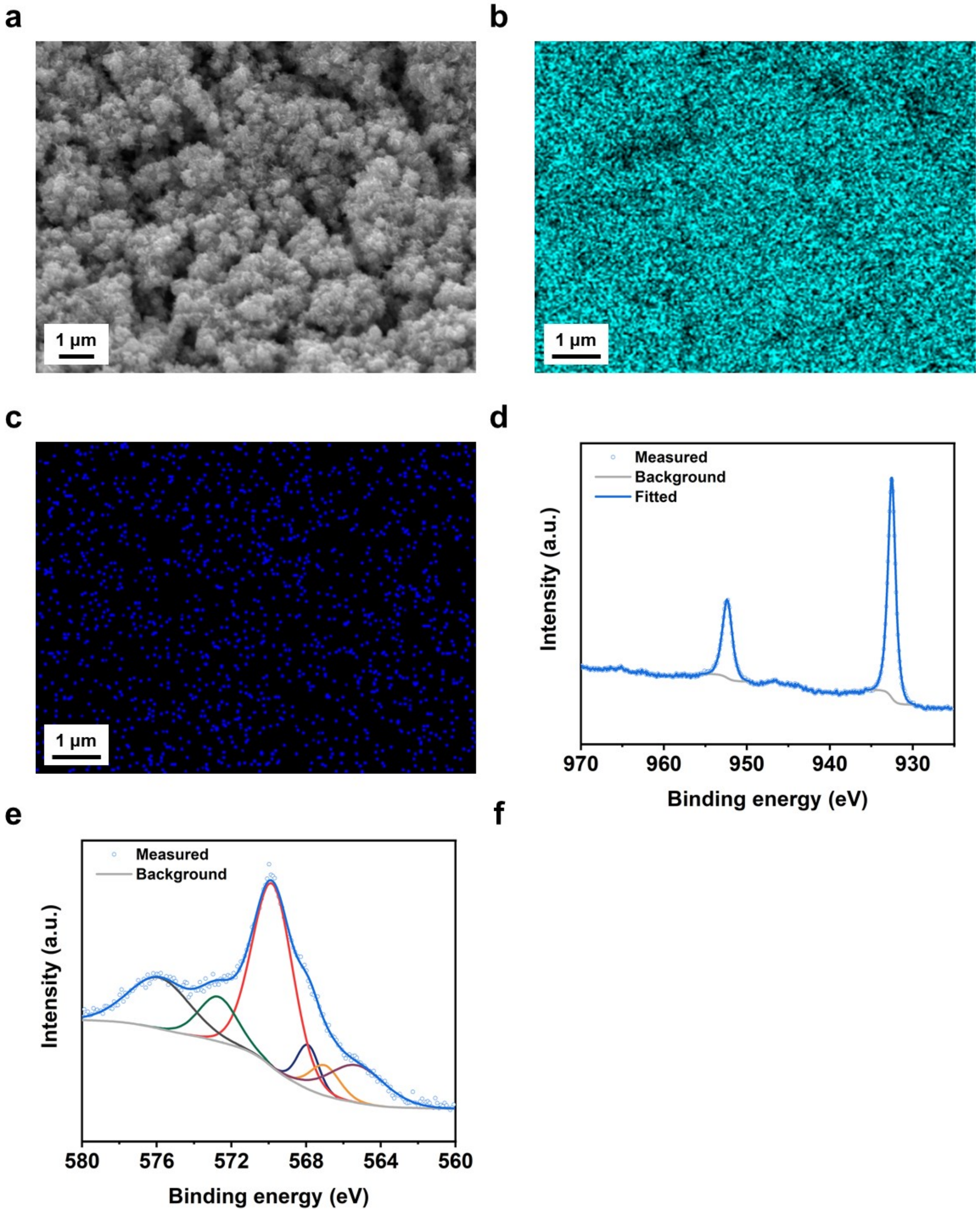

Figure S33. Ex-situ (a) FE-SEM image, and corresponding EDS elemental mapping of (b) Cu and (c) Pt of Pt-Cu/CF. Ex-situ (e) Cu 2p and (f) Cu LMM XPS spectra of Pt-Cu/CF after the stability test, all obtained from the anode side.

Table S1. Quantitative deconvolution of the Cu LMM Auger spectra.

Catalysts	Oxidation states	Binding energy (eV)	FWHM (eV)	Relative area (%)	Cu^0/Cu^+ ratio
Cu/CF	Cu^0	567.9	1.75	8.48	0.20
	Cu^+	569.8	2.15	41.42	
Co-Cu/CF	Cu^0	567.9	1.68	6.91	0.15
	Cu^+	569.8	2.00	45.50	
Pt-Cu/CF	Cu^0	567.9	2.00	11.20	0.28
	Cu^+	569.8	2.13	39.68	

* Relative area (%) denotes the fraction of the total Cu LMM Auger envelope area assigned to the main Cu^0 and Cu^+ components. Additional multiplet features were excluded from this quantification.

Table S2. Quantitative deconvolution of the Cu LMM Auger spectra after the half-cell stability test.

Catalysts	Oxidation states	Binding energy (eV)	FWHM (eV)	Relative area (%)	Cu^0/Cu^+ ratio
Co-Cu/CF (after FEH)	Cu^0	567.9	1.48	16.29	0.40
	Cu^+	569.8	2.31	40.65	
Co-Cu/CF (after FOR)	Cu^0	567.9	1.02	5.98	0.12
	Cu^+	569.8	2.56	51.66	
Pt-Cu/CF (after FEH)	Cu^0	567.9	1.52	13.14	0.36
	Cu^+	569.8	2.14	36.85	
Pt-Cu/CF (after FOR)	Cu^0	567.9	1.50	6.59	0.13
	Cu^+	569.8	1.92	51.66	
Cu/CF (after FEH)	Cu^0	567.9	1.55	15.03	0.39
	Cu^+	569.8	2.18	38.07	
Cu/CF (after FOR)	Cu^0	567.9	1.30	8.21	0.18
	Cu^+	569.8	2.32	45.33	

* Relative area (%) denotes the fraction of the total Cu LMM Auger envelope area assigned to the main Cu^0 and Cu^+ components. Additional multiplet features were excluded from this quantification.

Table S3. Quantitative deconvolution of the Cu LMM Auger spectra after the long-term stability test in the AEM co-electrolysis cell.

Catalysts	Oxidation states	Binding energy (eV)	FWHM (eV)	Relative area (%)	Cu^0/Cu^+ ratio
Pt-Cu/CF (cathode)	Cu^0	567.9	1.79	16.80	0.40
	Cu^+	569.8	2.10	41.81	
Pt-Cu/CF (anode)	Cu^0	567.9	1.38	5.94	0.13
	Cu^+	569.8	2.57	45.79	

* Relative area (%) denotes the fraction of the total Cu LMM Auger envelope area assigned to the main Cu^0 and Cu^+ components. Additional multiplet features were excluded from this quantification.

Table S4. Concentrations of dissolved metal ions (Cu and Pt) detected in the electrolyte by ICP-MS after the long-term stability tests.

Cycles	**Cathode (after FEH)**		**Anode (after FOR)**	
	Cu (ppb)	**Pt (ppb)**	**Cu (ppb)**	**Pt (ppb)**
1	6.022	0.017	1.259	0.026
2	1.110	0.015	1.423	0.023
3	1.329	0.019	1.304	0.016
10	1.125	0.017	1.484	0.019

Table S5. Comparison of the anodic potential at 10 mA cm^{-2} in FOR, UOR, and GOR reported in recent literature.

Substrate	Electrocatalyst	Electrolyte	Potential (vs RHE) @ 10 mA cm^{-2}	Ref
Formaldehyde	Pt-Cu/CF	1.0 M KOH + 0.6 M formaldehyde	0.012 V	Present work
	Cu_xO@CF	1.0 M KOH + 0.1 M formaldehyde	-0.07 V	[12]
	Ru/Cu-4	1.0 M KOH + 0.6 M formaldehyde	0.078 V	[13]
	CuFe	1.0 M KOH + 0.2 M formaldehyde	0.25 V	[14]
	Ag/Co_3O_4-R	1.0 M KOH + 0.5 M formaldehyde	0.32 V	[15]
	Cu	1.0 M KOH + 0.6 M formaldehyde	0.40 V	[16]
Urea	$Mn_xNi_{2-x}P$	1.0 M KOH + 0.5 M urea	1.24 V	[17]
	$Ni^{II+\delta}$-O-$Co^{II+\delta}$	1.0 M KOH + 0.33 M urea	1.288 V	[18]
	$Ni_2P_4O_{12}$/NiTe	1.0 M KOH + 0.33 M urea	1.313 V	[19]
	Fe-doped NiO	1.0 M KOH + 0.33 M urea	1.32 V	[20]
	NiO/CuO@CuM	1.0 M KOH + 0.5 M urea	1.35 V	[21]
	Ru-Ni_3N@NC	1.0 M KOH + 0.33 M urea	1.36 V	[22]
Glycerol	NiOOH/Ni_3S_2/NF	1.0 M KOH + 0.1 M glycerol	1.227 V	[23]
	$NiCoO_x$/CN_x-300	1.0 M KOH + 0.1 M glycerol	1.24 V	[24]
	HEA-CoNiCuMnMo	1.0 M KOH + 0.1 M glycerol	1.25 V	[25]
	Ni–Mo–N/CFC	1.0 M KOH + 0.1 M glycerol	1.30 V	[26]
	$Co_2(NiPcS_8)$	1.0 M KOH + 0.1 M glycerol	1.35 V	[27]
	Ni_3Fe	1.0 M KOH + 0.5 M glycerol	1.40 V	[28]

Reference

1 H. W. Huang, H. Jung, S. F. Li, S. Kim, J. W. Han and J. Lee, *Nano Energy*, 2022, **92**, 106763.

2 N. N. Zhang, R. Y. Zhu, S. L. Chen, N. Chen, Y. Q. Cao, L. Y. Ma, T. Wu and W. Sun, *Energy Fuels*, 2020, **34**, 742-748.

3 P. F. Brandao, R. M. Ramos, I. M. Valente, P. J. Almeida, A. M. Carro, R. A. Lorenzo and J. A. Rodrigues, *Anal. Bioanal. Chem.*, 2017, **409**, 2885-2892.

4 G. Kresse and J. Furthmuller, *Comput. Mater. Sci.*, 1996, **6**, 15-50.

5 G. Kresse and J. Furthmuller, *Phys. Rev. B*, 1996, **54**, 11169-11186.

6 G. Kresse and J. Hafner, *Phys. Rev. B*, 1993, **47**, 558-561.

7 G. Kresse and D. Joubert, *Phys. Rev. B*, 1999, **59**, 1758-1775.

8 J. P. Perdew, K. Burke and M. Ernzerhof, *Phys. Rev. Lett.*, 1996, **77**, 3865-3868.

9 P. E. Blochl, *Phys. Rev. B*, 1994, **50**, 17953-17979.

10 S. Grimme, J. Antony, S. Ehrlich and H. Krieg, *J. Chem. Phys.*, 2010, **132**, 154104.

11 G. Henkelman, B. P. Uberuaga and H. Jónsson, *J. Chem. Phys.*, 2000, **113**, 9901-9904.

12 Y. P. Pan, Y. Y. Li, C. L. Dong, Y. C. Huang, J. C. Wu, J. Q. Shi, Y. X. Lu, M. Yang, S. Y. Wang and Y. Q. Zou, *Chem*, 2023, **9**, 963-977.

13 S. Sarsenov, R. A. Senthil, A. Min, A. Kumar, C. J. Moon, J. Park and M. Y. Choi, *Small*, 2025, **21**, 2403999.

14 X. F. Gao, Y. P. Pan, J. H. Qiu, J. Peng, S. Y. Wang and Y. Q. Zou, *Adv. Funct. Mater.*, 2025, **35**, 2417545.

15 P. Y. Mao, B. B. Chen, R. Huang, Y. Jing, L. Xiao, B. H. Zhang and C. Shi, *Small*, 2024, **20**, 2405358.

16 G. D. Li, G. Q. Han, L. Wang, X. Y. Cui, N. K. Moehring, P. R. Kidambi, D. E. Jiang and

Y. J. Sun, *Nat. Commun.*, 2023, **14**, 525.

17 H. Yang, M. W. Yuan, D. Wang, Z. M. Sun, H. F. Li and G. B. Sun, *ACS Appl. Energy Mater.*, 2021, **4**, 8563-8571.

18 C. Y. Xie, C. H. Zhou, Y. Zhang, B. X. Zhou, Y. C. Yao, B. B. Li, J. H. Li, J. Bai, M. C. Long, K. Jiang, H. Zhu and L. Z. Zhang, *Angew. Chem. Int. Ed.*, 2026, **65**, e25119.

19 P. Guo, S. F. Cao, W. J. Huang, X. Q. Lu, W. Z. Chen, Y. Z. Zhang, Y. J. Wang, X. Xin, R. Q. Zou, S. B. Liu and X. H. Li, *Adv. Mater.*, 2024, **36**, 2311766.

20 H. K. Thakkar, K. H. Modi, K. K. Joshi, G. Bhadu, S. Siraj, P. Sahatiya, P. M. Pataniya and C. K. Sumesh, *ACS Sustain. Chem. Eng.*, 2024, **12**, 8340-8352.

21 L. L. Yang, R. He, X. Wang, T. T. Yang, T. Zhang, Y. Zuo, X. Lu, Z. F. Liang, J. S. Li, J. Arbiol, P. R. Martínez-Alanis, X. Q. Qi and A. Cabot, *Nano Energy*, 2023, **115**, 108714.

22 Y. B. Liu, D. B. Zheng, Y. Zhao, P. Shen, Y. X. Du, W. P. Xiao, Y. M. Du, Y. L. Fu, Z. X. Wu and L. Wang, *Int. J. Hydrog. Energy*, 2022, **47**, 25081-25089.

23 L. X. Xu, Y. F. Yang, C. Y. Li, R. Q. Ning, J. Ma, M. Q. Yao, S. Geng and F. Liu, *Chem. Eng. J.*, 2024, **481**, 148304.

24 B. K. Manna, R. Samanta and S. Barman, *ACS Appl. Energy Mater.*, 2024, **7**, 11787-11798.

25 L. F. Fan, Y. X. Ji, G. X. Wang, J. X. Chen, K. Chen, X. Liu and Z. H. Wen, *J. Am. Chem. Soc.*, 2022, **144**, 7224-7235.

26 Y. Li, X. F. Wei, L. S. Chen, J. L. Shi and M. Y. He, *Nat. Commun.*, 2019, **10**, 5335.

27 X. Huang, M. C. Wang, H. X. Zhong, X. D. Li, H. P. Wang, Y. Lu, G. P. Zhang, Y. N. Liu, P. P. Zhang, R. Q. Zou, X. L. Feng and R. H. Dong, *Angew. Chem. Int. Ed.*, 2025, **64**, e202416178.

28 Y. M. Li, H. L. Chen, F. Gao, Q. Chen, C. L. Li and J. F. He, *J. Colloid Interface Sci.*, 2025, **697**, 137913.